Lithos 386–387 (2021) 106043

Contents lists available at ScienceDirect

Lithos

journal homepage: www.elsevier.com/locate/lithos

Research Article

Differences in decompression of a high-pressure unit: A case study from the Cycladic Blueschist Unit on Naxos Island, Greece

Alexandre Peillod [a,*], Jarosław Majka [b,c], Uwe Ring [a], Kirsten Drüppel [d], Clifford Patten [e], Andreas Karlsson [f], Adam Włodek [c], Elof Tehler [a]

[a] Department of Geological Sciences, Stockholm University, Stockholm, Sweden
[b] Department of Earth Sciences, Uppsala University, Uppsala, Sweden
[c] Faculty of Geology, Geophysics and Environmental Protection, AGH University of Science and Technology, Kraków, Poland
[d] Department of Petrology, Karlsruhe Institute of Technology, Karlsruhe, Germany
[e] Department of Ore Geology, Karlsruhe Institute of Technology, Karlsruhe, Germany
[f] Department of Geosciences, Swedish Museum of Natural History, Stockholm, Sweden

ARTICLE INFO

Article history:
Received 10 November 2020
Received in revised form 1 February 2021
Accepted 3 February 2021
Available online 16 February 2021

Keywords:
Hellenide orogen
Cycladic Blueschist Unit
High-pressure metamorphism
Exhumation
Isobaric heating
Zr-in-rutile
Quartz-in-garnet (QuiG)
Thermodynamic modeling

ABSTRACT

Determining the tectonic evolution and thermal structure of a tectonic unit that experiences a subduction-related pressure temperature (P-T) loop is challenging. Within a single unit, P-T conditions can vary from top to bottom which can only be revealed by detailed petrological work. We present micropetrological data from the middle section of the Cycladic Blueschist Unit (CBU) in Naxos, Greece, which indicates a different P-T loop than that for the top of the sequence. Using Zr-in-rutile and Ti-in-biotite thermometry coupled with quartz-in-garnet elastic barometry and phase equilibrium thermodynamic modeling, we identify a prograde path from 15.4 ± 0.8 kbar to 19.9 ± 0.6 kbar and from 496 ± 16 °C to 572 ± 7 °C (2σ uncertainty), equilibration during decompression at 8.3 ± 1.5 kbar and 519 ± 12 °C followed by near-isobaric heating to 9.2 ± 0.8 kbar and 550 ± 10 °C (or even 584 ± 19 °C), and a final greenschist-facies equilibration stage at 3.8 ± 0.3 kbar and 520 ± 4 °C. We compare these P-T estimates with published data from the top and also the bottom of the CBU section and find that the bottom half of the CBU on Naxos records higher peak high-pressure (HP) of about 4 kbar than the top of the unit, defining the thickness of the CBU section on Naxos to about 15 km in the Eocene. We determine that crustal thickening of up to ~15% occurs in the upper half of the CBU section during exhumation of the HP rocks in an extrusion wedge in a convergence setting. At about 30 Ma, the bottom half of the CBU was finally thrust onto the radiogenic Cycladic basement. Subsequently this bottom half of the CBU section underwent isobaric heating of 9–96 °C between *c.* 32–28 and 23–21 Ma. Isobaric heating occurred below the upper CBU section that thickened during decompression and commenced when HP metamorphism in the Cyclades ended. This suggests that thermal relaxation following tectonic accretion in the Cyclades controlled heating of the evolving Cycladic orogen during a tectonically quiescent period before lithospheric extension commenced by 23–20.5 Ma.

© 2021 Stockholm University. Published by Elsevier B.V. This is an open access article under the CC BY license (http://creativecommons.org/licenses/by/4.0/).

1. Introduction

Exhumation of high-pressure (HP) rocks in subduction-zone settings often occurs in extrusion wedges (Chatzaras et al., 2006; Gessner et al., 2001; Glodny et al., 2008; Ring and Glodny, 2010; Xypolias et al., 2003). An extrusion wedge is defined by two main fault structures working in concert during overall horizontal lithospheric shortening: a thrust fault at the base of the wedge and a normal fault at its top, the latter of which facilitates exhumation. Deformation of an extrusion wedge can be localized on the two main faults exhuming the wedge passively as a coherent body without any significant change in wedge thickness. However, it is also possible that there is a series of thrust faults (e.g: Poulaki et al., 2019) or complex folding (e.g. Scheffer et al., 2016) in the wedge. Such internal structures would thicken the wedge. Conversely, there could be a series of normal faults at the top of the wedge thinning the wedge. Note that any thickening of an exhuming wedge needs to be less than the thinning at the top of the wedge along the upper normal fault(s). Moreover, in subduction zones the exhumation in extrusion wedges often occurs rapidly at rates close to the rate of subduction (Gerya et al., 2002; Ring and Reischmann, 2002; Rubatto and Hermann, 2001). Therefore, the typical time frame of 20–30 Ma needed for thermal relaxation (Glazner and Bartley, 1985) does not play a significant role (Peillod et al., 2017) and the extrusion wedge undergoes isothermal decompression or slightly cools during exhumation.

* Corresponding author.
E-mail address: alexandre.peillod@gmail.com (A. Peillod).

https://doi.org/10.1016/j.lithos.2021.106043
0024-4937/© 2021 Stockholm University. Published by Elsevier B.V. This is an open access article under the CC BY license (http://creativecommons.org/licenses/by/4.0/).

Early studies of the HP rocks of the Cycladic Blueschist Unit (CBU) showed pressure-temperature-time path (P-T-t) path encompassing Eocene (50–40 Ma) HP metamorphism followed by a Miocene (25–20 Ma) Barrovian-type overprint (see Jacobshagen et al., 1986; Okrusch and Bröcker, 1990 and references therein). More recent evidence reveals that HP metamorphism occurred at different times in distinct nappes of the CBU between about 55 and 30 Ma (see review in Ring et al., 2010) with diachroneous greenschist-facies overprints

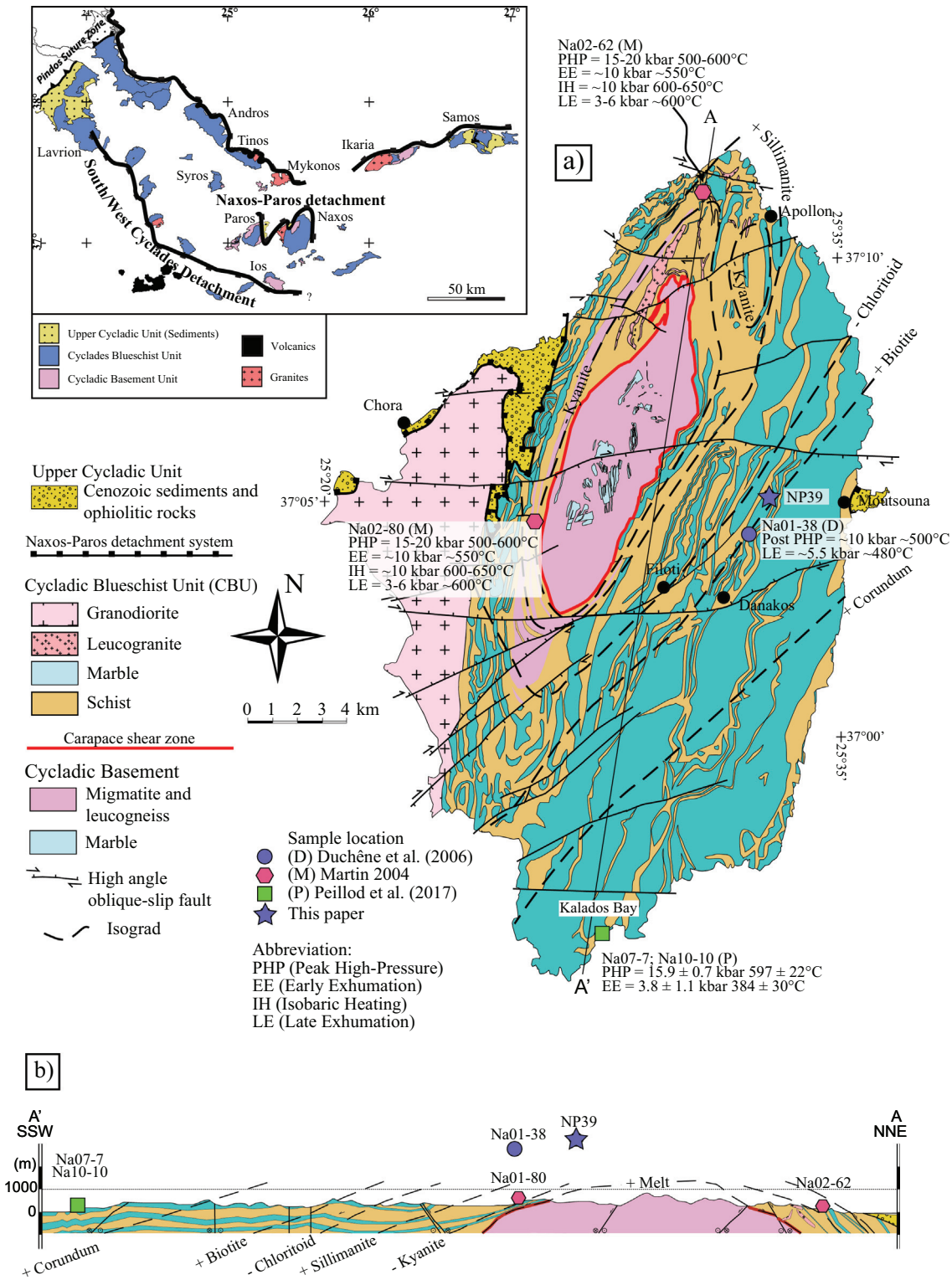

Fig. 1. a) Geological map of Naxos (modified from Jansen and Schuiling, 1976; Kruckenberg et al., 2010; Lamont et al., 2019; Vanderhaeghe, 2004) showing concentric isograd pattern around migmatite dome, sample locality of NP39 (blue star) and sample locations of previous petrology studies from CBU passive-margin sequence (purple pentagons, blue dot, green square). b) Cross-section showing domal architecture of Naxos with sample localities projected into cross-section plane. Inset: Simplified map of Cyclades with islands referred to in text and major detachments.

between about 40 to 12 Ma (see Ring et al., 2020, and references therein). Some studies suggested that during decompression a distinct thermal excursion defined by a phase of isobaric heating of about 50–150 °C occurred (Laurent et al., 2018; Parra et al., 2002; Ring et al., 1999; Trotet et al., 2001). The timing and tectonic control of this isobaric-heating stage is virtually unknown. Nonetheless, Huet et al. (2011) speculated that isobaric heating occurs locally during horizontal extension and is controlled by the inherited accretionary structure.

The island of Naxos in the central Cyclades is famous for its migmatite dome and the concentric pattern of Barrovian-type mineral isograds surrounding it (Fig. 1; Jansen and Schuiling, 1976). These isograds cut the tectonostratigraphic layering at moderate angles and serve here as structural markers within the CBU sequence. The main objective of this study is to constrain the P-T-t evolution of the middle CBU sequence near the biotite isograd for comparing it with two P-T-t paths from the bottom and the top of the CBU section, allowing to monitor the paleothickness evolution of the CBU during its exhumation. We show that the upper half of the CBU wedge, largly above the biotite isograd, below the bounding upper normal fault experienced continuous modest cooling during decompression between *c.* 40 ± 2 and 32 ± 2 Ma and thickened during exhumation while the CBU was thrust onto the Cycladic basement. Subsequently, the lower half of the CBU wedge below the biotite isograd experienced isobaric heating of 9–96 °C at ~9 kbar between *c.* 32–28 and 23–21 Ma. Our findings show that isobaric heating commenced immediately after the CBU was thrust onto the radiogenic Cycladic basement. At this time (*c.* 30 Ma), the final stages of HP metamorphism occurred in the Cyclades. Isobaric heating commenced after final thickening thrusting of the CBU onto the Cycladic basement and HP metamorphism, suggesting a causal relationship between these processes.

2. Geology of Naxos

Naxos is situated in the central part of the Cycladic archipelago (Fig. 1, inset), which is primarily be made up of the Permo-Carboniferous to latest Cretaceous passive-margin sequence of the CBU. Above the CBU is the Pelagonian Zone, remnants of which occur as klippen in the Cyclades. There are also Miocene sedimentary sequences tectonically above the CBU. Structurally below the CBU is the Cycladic basement, and also the Basal Unit as part of the External Hellenides.

The geology of Naxos can be subdivided from top to bottom into three units: (1) an Upper Unit containing Miocene non-metamorphosed sedimentary and ophiolitic rocks, (2) the CBU passive-margin sequence and, (3) the Cycladic basement (Fig. 1). The passive-margin sequence is mainly composed of alternating layers of marble, metapelite and metabasalt, with the metapelite layers more extensively exposed in the northern part and the marble in the southern part of the island (Fig. 1a). The Cycladic basement consists of migmatitic gneiss, leucogranite and marble.

Two major structures are recognized in Naxos (Fig. 1a). (1) The Miocene top-to-the-NNE Naxos-Paros extensional fault system with the underlying greenschist-facies to cataclastic Moutsouna shear zone (Andriessen et al., 1979; Brichau et al., 2006; Buick, 1991; Cao et al., 2018; Gautier et al., 1993). (2) A 500-m-thick shear zone straddling the basement/CBU contact, called the carapace shear zone by Listerand Forster (1996). This shear zone accommodated Oligocene trusting of the CBU onto the basement (Peillod et al., 2017) and was subsequently reactivated during Miocene extensional deformation under amphibolite-facies conditions (Lister and Forster, 1996; Vanderhaeghe, 2004). Extensional deformation controlled partial melting in the Cycladic basement forming the migmatite dome in the central part of Naxos, small leucogranite intrusions in the passive-margin sequence in NW-Naxos, and the large granodiorite intrusion in the west of the island (Buick and Holland, 1989; Jansen and Schuiling, 1976; Kruckenberg et al., 2011; Vanderhaeghe, 2004; Vanderhaeghe et al., 2007). Partial melting assisted deformation facilitating the large displacement of >80 km on the Naxos extensional fault system by drastically weakening the extending crust (Ring et al., 2018). Avigad et al. (1997), Kruckenberg et al. (2011) and Linnros et al. (2019) showed that migmatization was accompanied by *E*-W shortening coeval with NNE-SSW extension.

The metamorphic history of Naxos involves Eocene HP metamorphism, a subsequent Oligocene greenschist-facies overprint and a Miocene high-temperature (HT) event. Evidence for HP metamorphism is observed in Southeast Naxos at the top of the CBU sequence (Avigad, 1998; Lamont et al., 2019; Peillod et al., 2017). Peak HP conditions were calculated at >12 kbar and 470 ± 50 °C (2σ errors) using thermodynamic reactions (Avigad, 1998) and re-estimated at 15.9 ± 0.7 kbar 597 ± 22 °C using the Average P-T routine of the Thermocalc software package (Peillod et al., 2017) (Fig. 1a). A subsequent greenschist-facies equilibration stage at 3.8 ± 1.1 kbar and 385 ± 35 °C was calculated through univariant reaction lines Avigad, (1998) and the Average P-T method (Peillod et al., (2017) of Thermocalc. Lower in the sequence near the biotite isograd, Duchêne et al. (2006) reported garnet cores showing chemical signatures of HP metamorphism and subsequent rim growth. Using geothermobarometry, they calculated P-T conditions of ~10 kbar and ~500 °C followed by decompression to ~5.5 kbar and ~480 °C form post-HP garnet rims. At the bottom of the CBU sequence, Martin et al. (2006) argued that light REE-rich elements in epidote and $\delta^{18}O$ isotopes in garnet are indicative of HP metamorphism. Using the Theriak/Domino software, Martin (2004) estimated peak HP conditions of 15–20 kbar and 500–600 °C for samples Na02-62 and Na01-80 (Fig. 1a). The HP stage is followed by near-isothermal decompression to ~10 kbar, then isobaric heating from 550 to 600–650 °C, and a late decompression stage at 3–6 kbar and ~600 °C.

The Miocene HT metamorphic history was first studied by Jansen and Schuiling (1976) who mapped concentric metamorphic isograds recording increasing metamorphic grade toward the migmatite dome (Fig. 1a). The HT event is the dominant metamorphic overprint in large parts of the lower CBU and in the basement, the latter of which lacks any evidence for a preceding HP imprint. Based on geothermobarometry, Duchêne et al. (2006) estimated that peak P and T increased from 5 kbar and 470 °C in southern Naxos to 8 kbar and 700 °C close to the migmatite dome. Buick and Holland (1989), Peillod (2018), Ring et al. (2018) and Lamont et al. (2019) showed that the Miocene P-T path of the lowermost CBU and the Cycladic basement involved an early stage at *c.* 10 kbar and 650–680 °C associated with mineral assemblages containing kyanite, garnet and rutile. This stage was followed by near isothermal decompression with parageneses including sillimanite, garnet and ilmenite. Partial melting occurred at this decompression stage, which was followed by pronounced cooling when the isograds formed and the granodiorite intruded.

Peak HP metamorphism in Southeast Naxos is dated by Rb-Sr multi-mineral isochron ages between 40.5 ± 1.0 and 38.3 ± 0.5 Ma (Peillod et al., 2017). This age estimate is in line with Rb-Sr whole-rock + white-mica ages of *c.* 42 Ma on pristine HP rocks by Andriessen et al. (1979). Furthermore, Cao et al. (2017) obtained a $^{40}Ar/^{39}Ar$ total-fusion age of 38.3 ± 4 Ma for HP phengite from Central Naxos near the biotite isograd. In general, K-Ar and $^{40}Ar/^{39}Ar$ white-mica ages show a large scatter of ages for the HP event (Cao et al., 2018; Wijbrans and McDougall, 1986; Wijbrans and McDougall, 1988), which Andriessen et al. (1979) described to excess ^{40}Ar. Wijbrans and McDougall (1988) showed strong disequilibrium in white mica as expressed by upward convex age spectra. Wijbrans and McDougall (1986) proposed that the upward convex age spectra resulted from mixing of early HP phengite and later muscovite. Cao et al. (2018) reported significant disequilibrium in white mica due to either significant excess ^{40}Ar or from mixing of different white-mica populations. It is possible that both phenomena occurred rendering the detection of probable excess ^{40}Ar in HP white mica difficult. Given the widespread occurrence of excess ^{40}Ar in HP white mica, the youngest K-Ar and

$^{40}Ar/^{39}Ar$ white-mica ages, which are close to the Rb-Sr ages, are usually a good approximation of the true age of HP metamorphism (Ring et al., 2020; cf. Warren et al., 2012). Additional multi-mineral Rb-Sr ages indicate a minimum age of 38–36 Ma for blueschist-facies metamorphism near the biotite isograd in the middle CBU (Peillod et al., 2017). In the lower CBU, U-Pb zircon rim ages of 44 ± 3 Ma and 54 ± 6 Ma (Martin et al., 2006), and 40.1 ± 2 Ma (Bolhar et al., 2017) are interpreted to date zircon growth during HP metamorphism. Bolhar et al. (2017) and Peillod et al. (2021) argued that the older rim ages are probably contaminated by the older zircon cores and thus the youngest U-Pb zircon rim ages are close to the true age the metamorphic overprint. If so, the zircon rim ages are similar to the Rb-Sr ages of 42–38 Ma.

The greenschist-facies overprint of the blueschists in Southeast Naxos occurred in the Oligocene at 32 ± 3 Ma (Peillod et al., 2017). Zircon fission-track (ZFT) ages of 25.2 ± 3.8 and 20.5 ± 2.4 Ma constrain cooling through ~240 °C indicating that the top of the CBU sequence near Kalados Bay was in the brittle crust before the Miocene HT event commenced (Seward et al., 2009).

Keay et al. (2001) suggested that partial melting in the migmatite dome occurred between 20.7 ± 1 Ma and 17.4 ± 0.6 Ma and Vanderhaeghe et al. (2018) reported in-situ (SIMS) U-Pb zircon ages ranging from 24.2 ± 0.7 Ma to 16.6 ± 0.3 Ma from the migmatite. Ring et al. (2018) showed that the 20.7 ± 1 Ma age of Keay et al. (2001) is biased by inheritance and that an age of 18.4 ± 0.2 Ma from the same outcrop may reflect the first recorded crystallization of migmatite. The distinct peak of $^{206}Pb/^{238}U$ ages at *c.* 17.5 Ma for migmatite related zircon ages of Keay et al. (2001) appears to be the most robust and best age estimate for initial migmatite crystallization. Ring et al. (2018) also argued that the 24.2 ± 0.7 Ma apparent age of Vanderhaeghe et al. (2018) probably has contributions from old (Paleozoic) zircon cores and that zircon rim domains located in positions distal to old zircon crystal cores consistently show ages near *c.* 16 Ma, which seems to date termination of zircon forming processes in the migmatite.

Based on $^{40}Ar/^{39}Ar$ white mica and hornblende dating, Wijbrans and McDougall (1988) proposed that the peak of HT metamorphism occurred between 19.8 ± 0.2 and 15 ± 0.2 Ma. Wijbrans and McDougall (1988) argued that peak HT metamorphism probably occurred toward the lower end of this time span. This lower end correlates with U-Pb ages of zircon rims in amphibolite in the lower passive-margin sequence, indicating that conditions conducive to zircon growth during high-T have persisted at least until 15–14 Ma (Bolhar et al., 2017). Ring et al. (2018) reported Rb-Sr multi-mineral ages of pegmatite and migmatite demonstrating that HT metamorphic conditions and partial anatexis during top-to-the-NNE extensional shearing in the carapace shear zone lasted until about 14–12 Ma. Ductile shearing, fluid flow and recrystallization persisted until 10–8 Ma in North Naxos, based on $^{40}Ar/^{39}Ar$ dating of white mica (Cao et al., 2017). Jansen and Schuiling (1976) showed that the isograds formed after the peak of HT metamorphism, and Peillod (2018) and Ring et al. (2018) demonstrated that the isograds developed at a stage when the rocks started to cool considerably. Ring et al. (2018) argued for an age of about 14 Ma for isograd formation and Linnros et al. (2019) showed that the formation of the isograds proceeded from south to north during ongoing extensional deformation.

U-Pb zircon dating yielded ages between 15.4 ± 0.2 and 11.3 ± 0.4 Ma for S-type leuco- and biotite granites, and 13.2 ± 0.2 to 12.3 ± 0.2 Ma for the I-type granodiorite in western Naxos (Keay et al., 2001; Bolhar et al., 2010).Cao et al. (2017) reported $^{40}Ar/^{39}Ar$ white mica ages of 12.6 ± 0.6 Ma from the Moutsouna detachment shear zone at the eastern boundary of the metamorphic core complex, and 10.4 ± 0.9 Ma to 8.4 ± 1.5 Ma for ductile deformation along the Naxos extensional shear zone in northern Naxos. ZFT ages range from 25.2 ± 3.8 Ma in southern Naxos to 9.3 ± 2.8 Ma in northern Naxos. Apatite fission-track (AFT) ages range from 12 ± 7 Ma and 8.1 ± 2 Ma in the southern part of Naxos to 6.4 ± 1.8 Ma in the north (Brichau et al., 2006; Seward et al., 2009). Mancktelow et al. (2016) reported a K-Ar fault gouge age from the Naxos detachment of 9.7 ± 1 Ma.

3. Methods

This study focuses on one specific sample (NP39) from the middle CBU sequence close to the biotite isograd (Fig. 1a). NP39 shows remarkable garnets that record several stages of the prograde, peak and decompression history of the rock. Such garnets have already been reported from this unit (Duchêne et al., 2006) providing confidence that our sample is representative. To construct a P-T path, we combine in-situ quartz-in-garnet (QuiG) geobarometry and Zr-in-rutile and Ti-in-biotite geothermometry (Angel et al., 2019; Thomas et al., 2015; Wu and Chen, 2015). The intersection of the geobarometry and geothermometry isolines determine the P-T conditions of garnet growth. In addition, phase-equilibrium modeling using the Theriak/Domino software (de Capitani and Brown, 1987; de Capitani and Petrakakis, 2010) was used to calculate isopleths of garnet, white mica, biotite, chlorite and plagioclase, which supply independent P-T conditions for garnet growth from the previous methods. Phase-stability diagrams provide information about the stability of mineral assemblages because garnet had captured an incomplete set of the minerals from the matrix during HP conditions, and the later HT metamorphism most likely reequilibrated previous mineral assemblages in the matrix. Therefore, the rock lost part of its metamorphic history. Details of the methods are provided in Appendix A.1. All mineral abbreviations correspond to those in Whitney and Evans (2010).

4. Sample description

Sample NP39 is a strongly foliated garnet-biotite-bearing metapelite collected in eastern central Naxos close to the biotite isograd (37°05′11"N, 25°33′07″E; Fig. 1a). The mineral assemblage is garnet (3.8 vol %), white mica (29.1 vol%), feldspar (11.4 vol%), biotite (11.6 vol%), chlorite (3.8 vol%) and quartz (38.7 vol%), with minor epidote, tourmaline, rutile, zircon, ilmenite and apatite (1.6 vol%).

Two garnets (GrtA and GrtB) have been analyzed in detail. Garnet porphyroblasts are 1–1.5 mm in diameter (Fig. 2) and have triple rims (referred to as "inner", "central" and "outer" rims) surrounding the cores. Garnet cores are almandine rich ($Alm_{0.62}$ $Prp_{0.02}$ $Sps_{0.12}$ $Grs_{0.24}$ Fig. 2e; Table A.1). Compositional profiles of GrtA show an increase in almandine and pyrope content ($Alm_{0.61–0.62}$ $Prp_{0.02–0.03}$ to $Alm_{0.69–0.70}$ $Prp_{0.05–0.06}$) and a decrease in spessartine and grossular ($Sps_{0.09–0.10}$ $Grs_{0.24–0.26}$ to $Sps_{0.02–0.03}$ $Grs_{0.22–0.23}$) toward the inner rim. This is characteristic of garnet growth during prograde metamorphism (Fig. 2). A similar trend is observed for GrtB. We note that garnet cores and inner rims have similar composition profiles like those analyzed at Kalados Bay in South Naxos (Peillod et al., 2017). From inner to central rims, spessartine and almandine increase ($Sps_{0.02–0.03}$ $Alm_{0.69–0.70}$ to $Sps_{0.06}$ $Alm_{0.73–0.75}$), while grossular decreases ($Grs_{0.22–0.23}$ to $Grs_{0.15}$) and pyrope stays constant. Almandine and pyrope increase slightly from the central toward the outer rims ($Alm_{0.73–0.75}$ $Grs_{0.15}$ $Prp_{0.05–0.06}$ to $Alm_{0.76}$ $Grs_{0.16}$ $Prp_{0.07–0.08}$), while spessartine decreases ($Sps_{0.06}$ to $Sps_{0.01–0.02}$).

Differences in composition trends are observed between the central and outer rims for GrtA and GrtB, mainly for almandine and grossular composition. In GrtB, almandine decreases from the inner to the central rim ($Alm_{0.69}$ to $Alm_{0.54–0.55}$) while grossular increases ($Grs_{0.22–0.23}$ to $Grs_{0.27–0.28}$). Spessartine and pyrope follow the same trend as for GrtA with a more pronounced increase of spessartine ($Sps_{0.02–0.03}$, $Prp_{0.02–0.04}$ to $Sps_{0.16–0.17}$, $Prp_{0.02–0.04}$). From the central to the outer rim, almandine in GrtB shows first an increase and then a decrease ($Alm_{0.54–0.55}$ to $Alm_{0.68}$ to $Alm_{0.60}$); grossular increases ($Grs_{0.27–0.28}$ to $Grs_{0.31–0.34}$); spessartine decreases ($Sps_{0.16–0.17}$ to $Sps_{0.01}$) and pyrope remains constant.

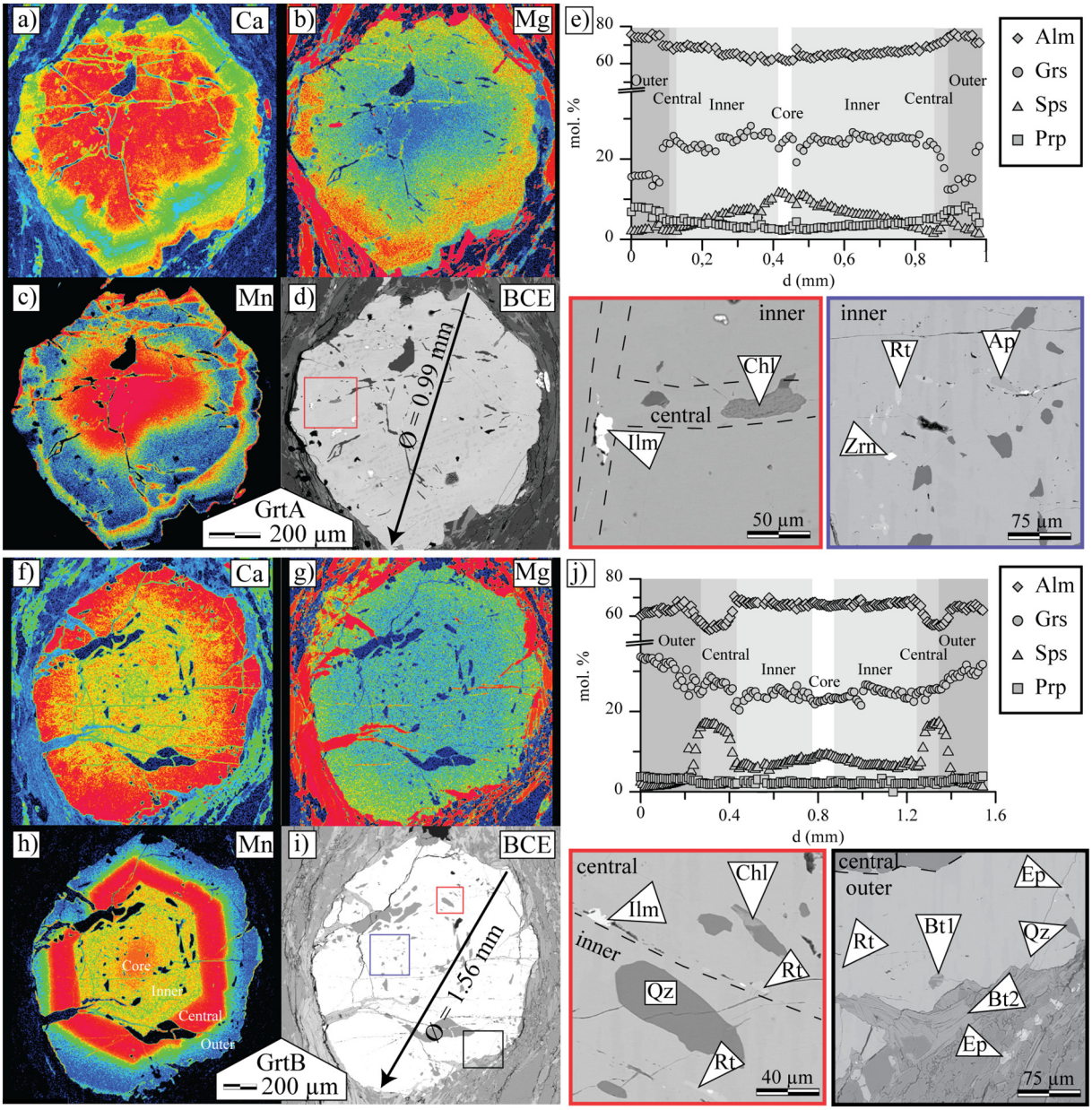

Fig. 2. Zoning maps (a-c and f-h), element profiles (e and j) of representative garnet porphyroblasts, and SEM images (d and i) of inclusions in garnet for NP39. X_{Fe} (Alm) = Fe/(Mg + Ca + Fe + Mn); X_{Ca} (Grs) = Ca/(Mg + Ca + Fe + Mn); X_{Mn} (Sps) = Mn/(Mg + Ca + Fe + Mn); X_{Mg} (Prp) = Mg/(Mg + Ca + Fe + Mn). Garnet core and rims defined by Mn composition maps and profiles.

These differences are supposed to be related to the timing of rim formation and the rim size. For example, spessartine content of the central rim is higher in GrtB than in GrtA because the composition map of Mn for this rim is larger in GrtB. Such behavior was described by George and Gaidies (2017) for garnet size populations. Additionally, it is possible that GrtB was cut in a way that the observed section does not pass through the center of this garnet, which could explain the Ca distribution for example. Therefore, we think that garnet core and inner rim compositions are better represented in GrtA, whereas the central and outer garnet rim compositions are better characterized in GrtB.

Garnet cores and inner rims host rutile, quartz, zircon and apatite inclusions (Fig. 2). The central rims contain rutile, quartz, ilmenite, chlorite and zircon, and outer rims have rutile, quartz, biotite and epidote inclusions (Fig. 2). The sizes of the inclusions is between 5 and 50 µm for most of the grains and ~ 200 µm for some quartz grains.

Fragments of garnet in the matrix most likely result from deformation (Fig. 3). Detailed observation of GrtA shows reveals multiple fractures filled by garnet of central rim composition and quartz suggesting that garnet broke soon after growth of the inner rim (Fig. 2a-d).

Two populations of white mica have been analyzed in the matrix (Figs. 3a and 4). One generation forms large crystals (>500 µm) with Si contents of 3.38–3.47 a.p.f.u. typical for HP metamorphism (Table A.2). This first generation has cleavage planes perpendicular to the matrix foliation suggesting that the cleavage in white mica is a relic foliation. However, it is difficult to know at which stage of HP phengite formed because no inclusions of phengite were observed in garnet. The second generation occurs as elongated fine grains along

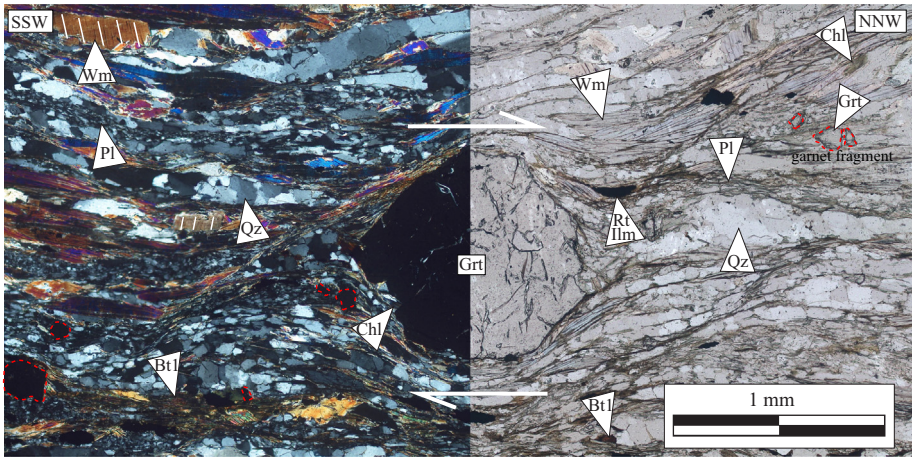

Fig. 3. Representative microstructures and metamorphic assemblages of sample NP39 in plane- (PPL) and cross-polarized light (XPL) showing orientation of different generations of white mica and dynamic recrystallization of quartz and plagioclase. Note plucked off and displaced garnet fragments in matrix. Also shown is top -NNW shear sense recorded by asymmetric strain caps around garnet.

the foliation (~200–500 μm) with Si contents of 3.08–3.09 a.p.f.u. and low Fe + Mg concentrations (0.07–0.08 a.p.f.u.).

Biotite has been analyzed in the outer garnet rim of GrtB. The Ti content is 0.07 a.p.f.u. and the Fe/Fe + Mg + Al^{VI} + Ti ratio is 0.4 (Table A.3). Two generations of biotite are observed in the matrix (Figs. 3 and 4b). Biotite1 is composed of large grains (>100 μm thick) which have a chemical signature close to the one analyzed in the garnet outer rim. The second generation (biotite2) consists of fine elongated grains along the foliation (100–500 μm) which started to replace garnet. The Ti content is lower than that of biotite1 (<0.06 a.p.f.u.) and the Fe/Fe + Mg + Al^{VI} + Ti ratio is increased (0.41–0.43). Feldspar is observed in the matrix in a 100 μm wide ribbon showing subgrain rotation recrystallization indicative of temperatures of ~550–600 °C (Fig. 3) (Stipp et al., 2002). Its composition is $Ab_{0.60–0.76}$ and $Kfs_{0.01}$ (Fig. 3c; Table A.4). Chlorite replaces garnet and biotite1 but is stable with biotite2 (Fig. 4). X_{Mg} of this chlorite is 0.49 (Table A.5). Rutile is preserved as inclusions in garnet and in the matrix (Figs. 2 and 4). Its Zr content increases from garnet cores to inner rims (from 7 to 67 ppm), then decreases to 7–22 ppm in central rims, before increasing again to 52 ppm in rutile in garnet outer rims (Table A.6). The latter value is similar to the one for rutile analyzed in the matrix and garnet cracks. Ilmenite is observed in garnet central rims together with rutile. In the matrix ilmenite is surrounded by rutile (Figs. 2 and 4). Quartz is observed as inclusions in garnet outer rims and in the matrix in a 100–300 μm wide ribbon. Quartz in his ribbon shows grain boundary migration recrystallization indicating temperatures >550 °C (Fig. 4) (Stipp et al., 2002). Locally subgrain rotation recrystallization affects the quartz rims reflecting the latest stage of ductile deformation.

5. P–T estimates

5.1. Geothermobarometry

Raman analyses were performed on quartz inclusions in GrtB. The calculated isomekes from the maximum Raman shifts and the isolines of the Zr-in-rutile and Ti-in-biotite thermometry are shown in Fig. 5 and Tables A.3; A.6 and A.7. P-T conditions are averages of the intersections of the isomekes and thermometry lines (Fig. 5, Table 1).

Quartz and rutile grains in garnet cores record average P and T of 15.4 ± 0.8 kbar and 496 ± 16 °C (Table 1; Fig. 5). Along the inner garnet rims, quartz and rutile grains document a P and T increase reaching peak HP at 19.9 ± 0.6 kbar and 572 ± 7 °C. Within garnet central rims, quartz and rutile records P-T condition of 9.4 ± 1.0 kbar and 497 ± 16 °C. In the outermost rims, quartz, rutile and biotite give average P-T of 9.2 ± 0.8 kbar and 550 ± 10 °C. Note that temperatures estimated from Ti-in-biotite thermometry for the single biotite inclusion in the GrtB outer rim yield 569 ± 65 °C for P fixed at 10 kbar (Table A.3). A similar temperature (~550 °C) is calculated for biotite1 in the matrix. For biotite2 in the matrix, Ti-in-biotite thermometry yields lower temperatures of 458–480 ± 65 °C for P of 4 kbar.

5.2. Thermodynamic modeling

For estimating prograde P-T conditions, compositional isopleths were calculated and compared to the composition of garnet cores ($Alm_{0.61–0.62}$, $Prp_{0.04}$, $Grs_{0.20–0.25}$, $Sps_{0.09–0.10}$) and its modal amount ($X_{Vol\%Grt}$ = 1.00–1.50%) (Fig. 6a). All calculated isopleths intersect

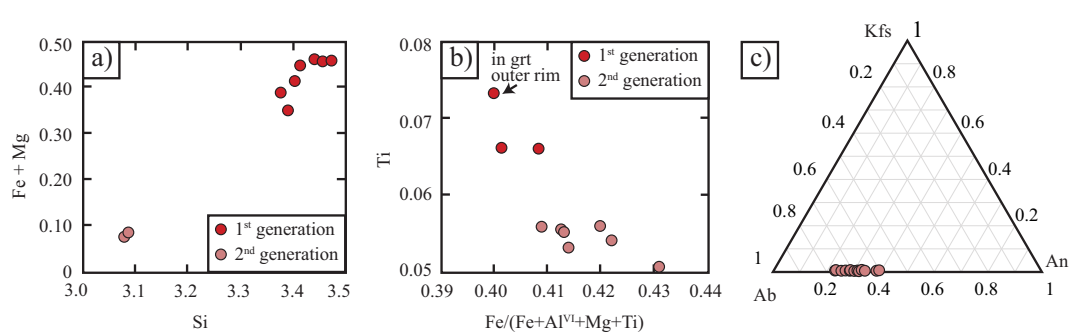

Fig. 4. a) Si vs. (Fe + Mg) diagram illustrating two types of white mica composition in matrix. b) Fe/Fe + Al^{VI} + Mg + Ti vs. Ti diagram for biotite composition in matrix and in garnet outer rims (Wu and Chen, 2015). c) Ternary diagram showing composition of feldspar in matrix.

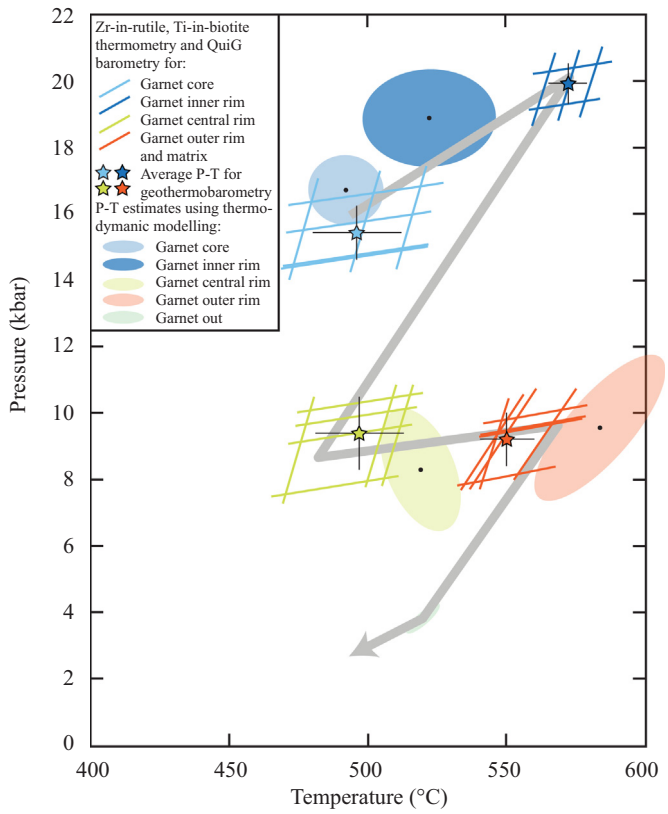

Fig. 5. P-T summary of Zr-in-rutile, Ti-in-biotite thermometry, Qtz-in-garnet barometry and pseudosection results. Dashed lines correspond to prograde data calculated for HP conditions (blue) and isobaric heating (red).

Table 1
Summary of P-T estimates from geobarometry based on Zr-in-rutile, Ti-in-biotite thermometry and quartz-in-garnet barometry, and from thermodynamic models.

Metamorphic stage	Thermodynamic models	Geothermobarometry
Prograde	16.7 ± 0.8 kbar	15.4 ± 0.8 kbar
garnet core	492 ± 11 °C	496 ± 16 °C
Peak high-P	18.9 ± 1.1 kbar	19.9 ± 0.6 kbar
garnet inner rim	520 ± 19 °C	572 ± 7 °C
Early exhumation	8.3 ± 1.5 kbar	<9.4 ± 1.0 kbar
garnet central rim	519 ± 12 °C	497 ± 16 °C
Isobaric heating	9.6 ± 1.8 kbar	9.2 ± 0.8 kbar
garnet outer rim	584 ± 19 °C	550 ± 10 °C
Late exhumation	3.8 ± 0.3 kbar	458–480 ± 65 °C
garnet out	520 ± 4 °C	for 4 kbar fixed

within the garnet + chlorite + white mica 1/2 + amphibole + rutile + lawsonite + quartz + H_2O stability field. These intersections yield average P-T conditions of 16.7 ± 0.8 kbar and 492 ± 11 °C (Table 1). Isopleths calculated for inner garnet rims ($Alm_{0.69–0.70}$, $Prp_{0.06}$, $Grs_{0.22–0.23}$, $Sps_{0.03–0.02}$, $X_{Vol\%Grt} = 2.00$) were used to estimate conditions of peak HP metamorphism. All calculated isopleths intersect within the garnet + white mica 1/2 + amphibole + chloritoid + rutile + lawsonite + quartz + H_2O stability field. The isopleth intersections yield average P-T conditions of 18.9 ± 1.1 kbar and 520 ± 19 °C (Fig. 6b; Table 1).

P-T conditions for formation of the garnet central rims are calculated using the composition of garnet ($Alm_{0.50–0.52}$, $Prp_{0.026–0.028}$, $Grs_{0.30–0.32}$, $Sps_{0.16–0.17}$; Fig. 6b) and of muscovite inclusions in these rims (Si-in-Ph = 3.10 a.p.f.u.). The calculated isopleths intersect within the stability field of garnet + biotite + chlorite + white mica 1/2 + rutile + epidote ± ilmenite + quartz + H_2O. Note that the two white mica models are muscovite and paragonite, the latter was not found in the sample. The isopleth intersections yield average P-T conditions of 8.3 ± 1.5 kbar and 519 ± 12 °C (Fig. 7a; Table 1).

P-T conditions for the outer garnet rims are calculated using the garnet composition ($Alm_{0.60–0.63}$, $Prp_{0.07–0.08}$, $Grs_{0.31–0.33}$, $Sps_{0.025}$ and $X_{Vol\%Grt} = 3.8$), the composition of phengite inclusions (Si-in-Ph = 3.09–3.10 a.p.f.u.) as well as the composition of biotite inclusions in outer rims ($X_{Mg} = 0.48$, Ti-in-biotite = 0.07 a.p.f.u.). Isopleths modeled for garnet, white mica and biotite compositions intersect within the stability fields of garnet + plagioclase + white mica 1/2 + rutile + epidote + quartz + H_2O. The isopleth intersections yield average P-T conditions of 9.6 ± 1.8 kbar and 584 ± 19 °C (Fig. 7b; Table 1).

P-T conditions for the assemblage postdating garnet formation are calculated from isopleths of albite (0.06), chlorite ($X_{Mg} = 0.49$) and biotite (Ti-in-Bt = 0.050–0.058 a.p.f.u.) in the matrix. The modeled isopleths intersect within the stability field plagioclase + biotite + chlorite + white mica 1 + ilmenite + quartz + H_2O and provide average P-T conditions of 3.8 ± 0.3 kbar and 520 ± 4 °C (Fig. 7b; Table 1).

5.3. Summary

The P-T estimates are summarized in Table 1. For the formation of garnet cores, thermodynamic modeling defines a prograde stage at 16.7 ± 0.8 kbar and 492 ± 11 °C, followed by peak HP metamorphism at 18.9 ± 1.1 kbar and 520 ± 19 °C. At these P-T conditions, stable assemblages reveal the occurrence of glaucophane, paragonite, lawsonite, chlorite and chloritoid which are not observed in sample NP39. These phases are observed in samples which better preserve the HP mineralogy in Naxos (Andriessen et al., 1979; Jansen and Schuiling, 1976; Wijbrans and McDougall, 1988). The pronounced lower-P overprint observed in NP39 most probably fully obliterated glaucophane, paragonite, lawsonite and chloritoid in the matrix. However, this does not justify the absence of those minerals as inclusion in garnet. It is most likely that the numerous fractures observed in GrtA are from dehydration of hydrous minerals like lawsonite, chlorite, glaucophane and chloritoid at near peak HP conditions. Such a case has been described in the Scandinavian Caledonides in rocks that experienced a similar P-T history than that recorded in NP39 (Bukała et al., 2020). Alternatively, the garnet fractures, resulting from volume change during decompression, allowed fluids to reequilibrate hydrous minerals trapped in garnet.

The P-T conditions for the prograde stage as determined from thermodynamic modeling and calculated from rutile-quartz geothermobarometry agree well with each other. For peak HP conditions, however, the discrepancy between the modeling and the geothermobarometry data is not negligible. The temperature for peak HP conditions from modeling is ~50 °C lower than estimated from rutile-in-quartz geothermobarometry. We think that the modeled peak HP temperature is shifted to lower values because of a depletion of certain elements (e.g. Mg) which are fractionated by other mineral phases (e.g. glaucophane) that grew together with garnet. These phases completely reequilibrated during decompression which led to a lack of control of mineral fractionation in our model resulting in the observed temperature shift. The missing control of the mineral fractionations to calculate the effective bulk-rocks composition of each rims of our model caused the observed temperature shift. P-T conditions estimated from rutile thermometry and QuiG are thus considered more accurate.

Garnet central rims record an early exhumation stage at 9.4 ± 1.0 kbar and 497 ± 16 °C as determined from thermobarometry data. Within errors, this result fits with the results obtained from thermodynamic modeling, which yield 8.3 ± 1.5 kbar and 519 ± 12 °C. However,

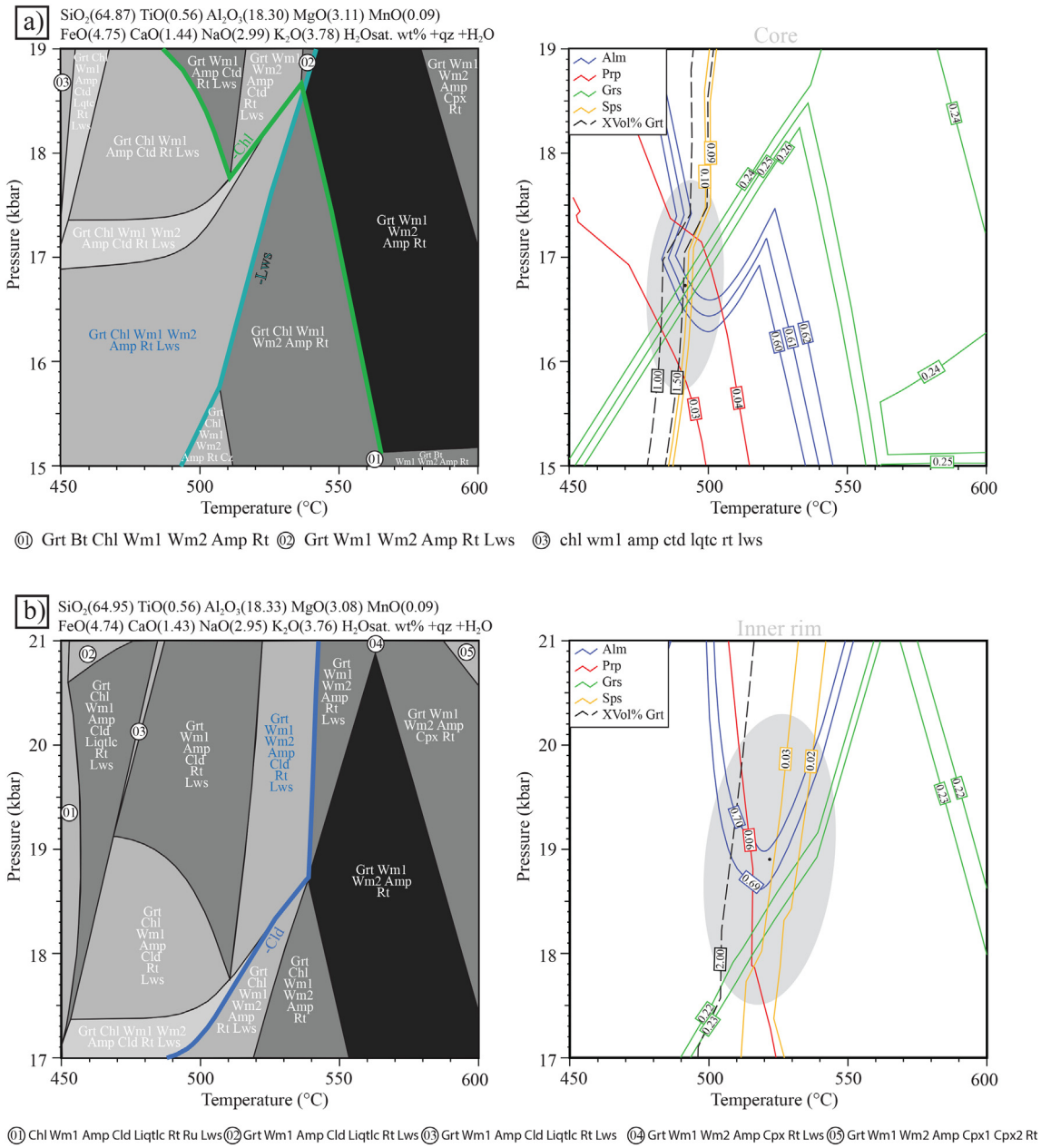

Fig. 6. P-T pseudosections of NP39 calculated for prograde P-T path in MnNCKFMASHTO system. a) Left-hand side: Pseudosections calculated for prograde P-T conditions; right-hand side: P-T conditions estimated from intersections of garnet core composition isopleths and modal abundance of garnet. b) Left-hand side: Pseudosection calculated for peak P-T conditions. Right-hand side: Peak HP conditions, estimated from intersections of garnet core composition isopleths and modal abundance of garnet. Possible mineral assemblages corresponding to P-T stages highlight in blue. Mineral abbreviations according to Whitney and Evans (2010).

we think that P obtained from the thermodynamic modeling is more accurate, because no quartz inclusions were analyzed within the outermost part of the central rim and therefore the P estimates define maximum P for the formation of the garnet central rim. Therefore, we prefer P-T conditions of 8.3 ± 1.5 kbar and 519 ± 12 °C from thermodynamic modeling.

For the formation of garnet outer rims, rutile and biotite thermometry implies a continuous prograde T increase to 550 ± 10 °C at 9.2 ± 0.8 kbar as obtained by QuiG barometry. The increase in T would be between 9 and 53 °C. This P-T data of 550 ± 10 °C at 9.2 ± 0.8 kbar overlap with those obtained from the pseudosections (i.e. 9.6 ± 1.8 kbar, 584 ± 19 °C). Including the T estimates from both geothermobarometry and the pseudosections, we calculate that NP39 experienced a T increase of 9–96 °C. P-T conditions of the latest stage after garnet breakdown were estimated from pseudosections at 3.8 ± 0.3 kbar and 520 ± 4 °C.

6. Tectonic implications

6.1. From top to bottom, P-T-t paths for the CBU passive-margin sequence

We combine the P-T with the geochronologic data and compare a published P-T-t path from the top of the exposed CBU section at Kalados Bay (Peillod et al., 2017) and one derived from samples Na02-80 and Na02-62 (Martin, 2004) from the bottom of the CBU sequence (Fig. 1a) with the here reported P-T-t data of sample NP39 from near the biotite isograd.

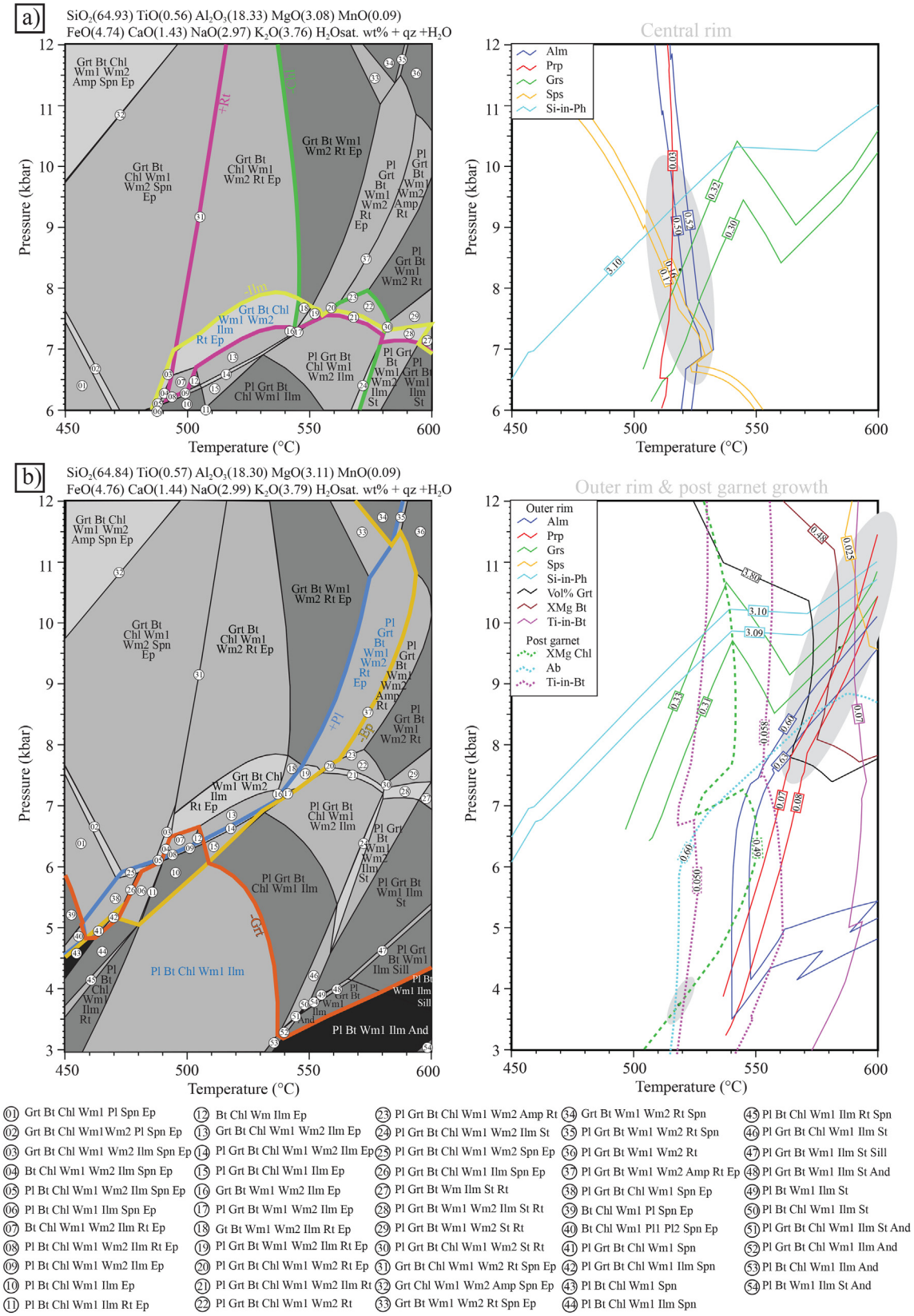

Fig. 7. Retrograde P-T evolution of NP39, a) Left-hand side: Pseudosection of early retrograde P-T conditions, calculated in MnNCKFMASHTO system. Right-hand side: P-T conditions, calculated from intersections of isopleths of garnet central rim composition and white mica. b) Left-hand side: Pseudosection of late retrograde P-T conditions, calculated in MnNCKFMASHTO system. Right-hand side: P-T conditions, calculated from intersections of isopleths of garnet outer rim composition and white mica and biotite. P-T conditions agree well with those of mineral assemblage postdating garnet growth, as calculated from composition of matrix chlorite, albite, and biotite. Mineral abbreviations according to Whitney and Evans (2010).

6.1.1. Top of CBU sequence: Kalados Bay

The P-T-t path for Kalados Bay at the top of the CBU sequence is well constrained (Fig. 8). The rocks experienced peak HP conditions of 15.9 ± 0.7 kbar and 597 ± 22 °C (Fig. 8) at *c.* 42–38 Ma (Andriessen et al., 1979; Peillod et al., 2017). The greenschist-facies overprint at 3.8 ± 1.1 kbar and 384 ± 30 °C (Avigad, 1998; Peillod et al., 2017) occurred at 32 ± 3 Ma (Andriessen et al., 1979; Peillod et al., 2017), constraining near-isothermal decompression to between about 40 ± 2 and 32 ± 3 Ma. ZFT ages of 25.2 ± 3.8 and 20.5 ± 2.4 Ma (Seward et al., 2009) indicate that the top of the sequence moved thought the brittle-ductile transition near the Oligocene/Miocene boundary.

6.1.2. Middle CBU sequence: Sample NP39

Lower in the CBU section, our P-T estimates for NP39 provide a distinctly more complicated P-T path than that observed at the top of the sequence at Kalados Bay (Fig. 8). P-T conditions for peak HP (19.9 ± 0.6 kbar, 572 ± 7 °C) are slightly higher than for Kalados Bay. No direct data constraining the age for peak HP metamorphism of NP39 exist. However, the age of 38.3 ± 4 Ma for HP phengite by Cao et al. (2017) is from a locality near the sampling site for NP39. Furthermore, multi-mineral Rb-Sr isochron data for samples collected from the same locality as NP39 (NAX15-14) or from nearby localities (NAX15-13 and NAX15-20) (reported in Peillod et al., 2017) provided ages between 38 and 36 Ma, which were interpreted as minimum ages for the end of blueschist-facies metamorphism. In addition, $^{40}Ar/^{39}Ar$ step-heating data on white-mica grain-size fractions >250 μm from NAX15-14 gave an age of 38 ± 1 Ma for the end of HP metamorphism (Peillod et al., 2019). The latter age overlaps with those obtained from Kalados Bay. Therefore, it is likely that prograde and peak HP of sample NP39 occurred at the same time as at Kalados Bay (Fig. 8).

An exhumation stage of NP39 was estimated at 8.3 ± 1.5 kbar and 519 ± 12 °C. Multi-mineral Rb-Sr age data from NAX15-14 provided an age of 31.8 ± 0.5 Ma, interpreted as a maximum age for the end of decompression. Duchêne et al. (2006) reported a slightly younger Rb-Sr whole rock-phengite-garnet age of 29.3 ± 1.3 Ma (their sample Na01-38). Based on those two ages, we consider an age of 32–28 Ma reasonable for the switch from decompression to isobaric heating.

The next step of the P-T loop is isobaric heating from 519 ± 12 °C to 550 ± 10 °C (maximum would be 584 ± 19 °C) at ~9 kbar after the early decompression stage. Geochronologically constraining the isobaric-heating stage is challenging. The above reported ages for the end of the decompressional stage also reflect the onset of isobaric heating, i.e.

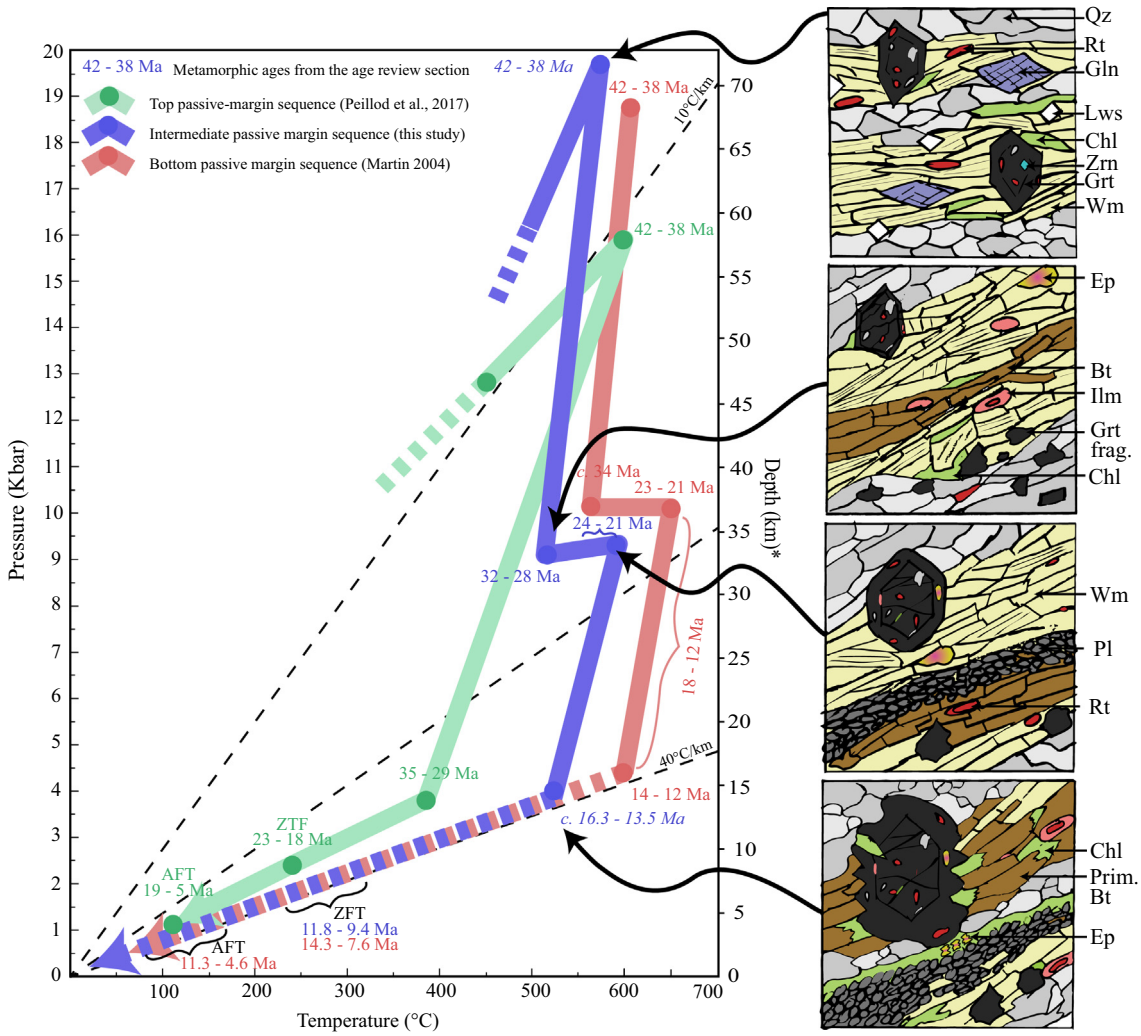

Fig. 8. Pressure-temperature-time (P-T-t) path for sample NP39 with available age data. Also shown P-T-t paths from Kalados Bay (green; Peillod et al., 2017) at top, and samples Na02–80 and Na02–62 (red; Martin, 2004) from base of Naxos CBU section with ages, inferred ages in italics. P converted to depth assuming average rock density of 2800 kg/m^3 (Semprich et al., 2010). On right, evolution of metamorphic assemblage during exhumation of NP39 (refer to petrological description for schematic evolution of metamorphic assemblage). Mineral abbreviations according to Whitney and Evans (2010); Frag. (fragment), Prism. (prismatic).

32–28 Ma. The end of isobaric heating constraints the beginning of peak temperature conditions of NP39. This stage might be best represented by an $^{40}Ar/^{39}Ar$ hornblende plateau age of 23.1 ± 1 Ma, interpreted as amphibole reequilibration at commencing HT metamorphic conditions by Wijbrans and McDougall (1988; their sample 81.540). Cao et al. (2018; sample N11B-exp2) interpreted an $^{40}Ar/^{39}Ar$ step-heating age of *c.* 24 Ma from phengite/muscovite single grains to reflect a thermal pulse predating the Miocene HT event. $^{40}Ar/^{39}Ar$ step-heating data on white mica for NAX15-14 yielded an age of *c.* 21 Ma for the onset of the HT stage (Peillod et al., 2019). From all this we infer that isobaric heating in sample NP39 ended by 24–21 Ma (Fig. 8). HT metamorphism was a protracted event persisting on Naxos until about 14–12 Ma (Ring et al., 2018; Wijbrans and McDougall, 1988).

Isobaric heating was followed by a second near-isothermal decompression stage from 9.2 ± 0.8 kbar and 550 ± 10 °C to 3.8 ± 0.3 kbar and 520 ± 4 °C. A $^{40}Ar/^{39}Ar$ hornblende plateau age of 16.1 ± 0.2 Ma represents an age for the end of HT metamorphism (Wijbrans and McDougall, 1988, sample 81.564). Furthermore, Cao et al. (2017, sample N1A) provided a well-defined $^{40}Ar/^{39}Ar$ white-mica plateau age of 14.3 ± 0.8 Ma for the end of HT conditions. Based on this, we consider ages between 16.3 and 13.5 Ma to represent the end of HT conditions near the biotite isograd. ZFT data for sample H11 of Seward et al. (2009) from a locality close to NP39 gave an age of 10.6 ± 1.2 Ma (Fig. 8).

6.1.3. Bottom of CBU sequence: Samples Na02-80 and Na02-62

At the bottom of the passive-margin sequence, Martin (2004) produced a P-T path, which is strikingly similar to that of NP39 (Fig. 8). Note that sample Na02-80 is from the very bottom of the CBU section and Na02-62 from close to the bottom (from between the kyanite and sillimanite isograds, Fig. 1a); the P-T path reported by Martin (2004) represents a composite path for both samples. This composite path defines peak HP conditions at 15–20 kbar and 500–600 °C, followed by near-isothermal decompression to ~550 °C ~ 10 kbar, in turn succeeded by isobaric heating from 550 to 600–650 °C, and a final decompression stage at 3–6 kbar and ~ 600 °C.

Martin et al. (2006) combined data on linked HP zircon and garnet growth with $\delta^{18}O$ isotopes and assigned a U-Pb zircon rim age of 44 ± 3 Ma to the peak HP event. Bolhar et al. (2017) reported additional U-Pb zircon rim ages of 40.7 ± 2 Ma and 39.6 ± 1.1 Ma for samples near Na02-62. Martin et al. (2006) reported U-Pb zircon rim ages of *c.* 34 Ma, which reflect an early decompression stage of the HP rocks. HT metamorphism and anatexis occurred between 18 Ma and 14–12 Ma (Ring et al., 2018) after the onset of extensional shearing starting at 23–20.5 Ma (Brichau et al., 2006; Cao et al., 2017; John and Howard, 1995; Mancktelow et al., 2016; Seward et al., 2009). The latter ages reflect the end of the isobaric heating stage.

6.1.4. Summary

The shapes of the P-T-t paths show differences between the top and the bottom part of the CBU sequence. (1) The most drastic difference is that the top of the CBU sequence shows a "standard" P-T-t loop for exhumed HP rocks in subductions settings, whereas the rocks from the bottom half show an isobaric-heating stage during exhumation. In other words, the top-half rocks decompressed and slightly cooled during most of their exhumation history, whereas the bottom half underwent a thermal excursion on the way up at ~35 km depth at a time when the top of the sequence was already close to the brittle-ductile transition at 32 ± 3 Ma (at about 13 km depth according to the barometric estimates). Note that the P-T-t history for the entire bottom half of the CBU section appears to be rather similar, even if the path for the bottom as deduced from samples Na02-80 and Na02-62 is composite and based on crude P-T estimates. (2) The top of the CBU experienced lower peak HP conditions than the bottom half at 40 ± 2 Ma, which appears reasonable as samples NP39, Na02-80 and Na02-62 are derived from deeper parts of the subducted CBU nappe. (3) The top of the sequence moved through the brittle-ductile transition near the Oligocene/Miocene boundary while the bottom of the sequence started to be (re)exhumed at about the same time (23–21 Ma). This exhumation was due to the inception of the Naxos extensional fault and near-isothermal decompression of the bottom half of the CBU sequence occurred at HT conditions during the early and middle Miocene (from about 23–21 to 14–12 Ma) accompanied/followed by pronounced cooling and movement through the brittle-ductile transition. Extensional deformation finally juxtaposed the currently outcropping CBU rocks on Naxos.

6.2. Exhumation and cooling rates of the CBU sequence

The data show that the rocks from the bottom half of the passive-margin sequence record a different P-T-t evolution than those at the top, resulting in different exhumation and thermal regimes. Based on the information provided in Fig. 8, P-t and T-t paths were constructed (Fig. 9) and averaged exhumation and cooling rates were calculated.

The early exhumation rate for NP39 is 5.3 ± 2.5 km/Ma between 40 ± 2 and 32 ± 3 Ma, followed by a stage of no exhumation (−0.3 ± 0.6 km/Ma) between *c.* 32 and 21 Ma during isobaric heating. The second exhumation shows an initial exhumation rate of 2.2 ± 0.5 km/Ma between *c.* 21 and 15 Ma, similar to 2.1 ± 1.6 km/Ma between *c.* 15 and < 10 Ma.

The T-t path of NP39 gives an initial cooling rate of 7 ± 3 °C/Ma between 40 ± 2 and 32 ± 3 Ma, then heating at a rate of −5 ± 4 °C/Ma from *c.* 32 to 21 Ma. The second cooling was initially at 6 ± 4 °C/Ma between *c.* 21 and 14 Ma and strongly increased to 117 ± 79 °C/Ma between *c.* 12 and 11 Ma.

We compare the exhumation and cooling rates for the middle CBU sequence (NP39) with those reported in Peillod et al. (2017) for the top and those calculated from the Martin (2004) data. At the start of exhumation all rocks across the entire CBU sequence show similar P-t paths and early exhumation rates are comparable. At about *c.* 32 Ma at 9 kbar (~33 km depth) the paths diverge and the bottom half of the sequence stops exhuming, while the top of the sequence keeps exhuming at a constant rate. The exhumation paths then converge again at about 11–13 Ma at shallow crustal levels of about 3 kbar (~11 km depth) in the upper crust.

The cooling rates are more disparate (Fig. 9). The top of the sequence cools fairly steadily with a small kink at about *c.* 32 Ma. The bottom half of the CBU exhumes nearly isothermally before being heating between *c.* 32 and 21 Ma, this heating is slightly more pronounced at the bottom as manifested by higher peak temperatures of ~625 °C (Figs. 8, 9). Significant cooling starts at about 23–21 Ma related to the onset of extensional faulting.

6.3. Structural thickness changes of the CBU sequence during exhumation

We discuss how the different P-T-t paths relate to structural thickness changes of the CBU section during its exhumation in an extrusion wedge. The baric data from the top, middle and bottom of the CBU sequence are of different quality, allowing only to make crude thickness estimates. For simplicity, we divide the CBU section into a top and a bottom half, both of which are largely separated by the biotite isograd. We admit that this is a simplified approach, which we justify by the sparse data set that shows pronounced differences between the two halves.

This thickness at peak HP metamorphism as deduced from the P difference of about 4 kbar between top and bottom is 15 km (Fig. 10). This estimate is crude as the P data from Martin (2004) are not accurate and no errors are reported. However, peak P of Martin (2004) is similar to peak P estimated for NP39. The thickness difference of the upper half of the CBU section between NP39 and Kalados Bay would be more accurate at 14.6 ± 1.9 km (4.0 ± 0.5 kbar). At ~32–28 Ma, the bottom half of the sequence was at 8.3 ± 1.5 kbar, while the top of the unit was at 3.8 ± 1.1 kbar (Fig. 10) suggesting that the thickness during wedge

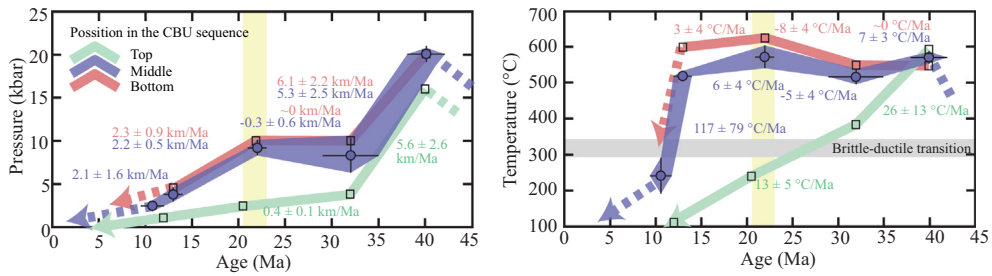

Fig. 9. Exhumation (P-t) and cooling (T-t) path for top (Kalados Bay), middle (NP39) and bottom (Na02-62 and NP02-80) CBU sequence. Onset of extension at 23–20.5 Ma shown by vertical yellow bar; exhumation and cooling rates for Kalados Bay recalculated from Peillod et al. (2017).

extrusion increased to 16.4 ± 3.3 km (~15%). Because the P-T-t paths for the bottom half of the CBU do not differ much, this thickness change occurred basically in the upper half of the extruding CBU wedge. Note that because of the errors the thickness may not have changed at all but may have increased by about 7 km.

A potential increase in crustal thickness cannot be explained by a passively extruding wedge and requires internal thickening of the wedge during extrusion. This thickness increase could have been accommodated by a single thrust fault or a succession of thrust faults. A single fault would have generated a wide shear zone which is so far not observed in Naxos and not supported by the regional geology (Peillod et al., 2021; but see Lamont et al. (2019) for different interpretation). A succession of thrust faults would have resulted in more discrete shear zones. Based on detrital U-Pb zircon ages defining a sequence of km-thick metasediments slices, Poulaki et al. (2019) suggested a series of internal thrusts on Ios Island. In line with this proposition, we suggest that a series of relatively small displacement thrusts thickened the upper half of the CBU sequence (i.e., above sample NP39) during exhumation of the HP rocks.

6.4. Relation between Oligocene isobaric heating and the Miocene migmatite dome

Peillod et al. (2017) showed that the CBU passive-margin sequence was thrust onto the Cycladic basement at *c.* 30 Ma. Lithospheric extension commenced at 23–20.5 Ma as deduced from the age of the supradetachment sediments (Angelier et al., 1982; Lisker, 1993). The timing constraints show that isobaric heating occurred between 32 and 28 and about 24–21 Ma, which is basically the time between emplacement of the CBU above the basement and the start of lithospheric extension before the peak of HT metamorphism was at about 18–14/12 Ma.

The basal section of the CBU stayed above the granitic (radiogenic) basement for about 4–11 Myr. However, the basal CBU section now exposed on Naxos was not above the Naxos Cycladic basement between 32 and 28 and 24–21 Ma and was later emplaced on this basement during lithospheric extension along the carapace shear zone. The total extension at the Naxos extensional fault system was >80 km (Brichau et al., 2006) but the displacement at the carapace shear zone is unknown. Because the Cycladic basement is also widely exposed on Ios Island south of Naxos, it is likely the basal CBU section was above basement during the 4–11 Myr period.

Over this period of time typical values for isobaric heating would be 40–90 °C as calculated from numerical models (Bucher and Grapes, 2011; England and Thompson, 1984). We envisage that radioactive decay within the basement caused the temperature increase of 9–96 °C in the directly overlying basal CBU section (Fig. 10). Radioactive decay may have also increased temperatures in the basement itself ultimately aiding migmatization and protracted HT metamorphism. The temperature increase over ~4–11 Ma decreases the lithospheric strength by about 25–40% causing lithospheric weakening (Glazner and Bartley, 1985).

Isobaric heating starting at 32–28 Ma cannot be due to lithospheric extension in the back-arc region of the Hellenic subduction zone as it occurred before extension started. There is evidence for HP metamorphism on Evia and Sifnos at about 30 Ma (Ring et al., 2007; Ring et al., 2011), and also evidence for thrust deformation, for instance on Syros between about 30 and 27 Ma (Aravadinou and Xypolias, 2017; Ring et al., 2020) and on Crete (Fassoulas, 1998). As proposed by Peillod et al. (2021), we envisage that the CBU and the Cycladic basement was not deforming significantly between about 30 and 23–20.5 Ma and was slowly eroding over this period of time.

Extensional deformation commencing by 23–20.5 Ma caused the final exhumation of the CBU sequence on Naxos (second exhumation in Fig. 10). At this stage, the top-CBU sequence kept cooling and decompression rather continuously. The central and bottom CBU started to be decompressing but hardly cooled at all until about 13–11 Ma (Figs. 8, 9). The lack of significant cooling of the bottom half of the CBU might be due to intrusion of granites and pegmatites until about 13–12 Ma (Keay et al., 2001; Bolhar et al., 2010; Ring et al., 2018).

6.5. Extent of isobaric heating in the Cyclades

Across the Cyclades, isobaric heating has previously been described from a few other islands. On Samos, Ring et al. (1999) described isobaric heating from 380400 to 450–490 °C at ~7 kbar during the exhumation of the HP rocks. On Andros, a similar thermal overprint is reported from ~300 °C to 400–430 °C at ~7 kbar (Huet et al., 2015). On Syros, Laurent et al. (2018) suggested isobaric heating of ~70 °C from 500 to 570 °C at ~10 kbar. On the Lavrion peninsula, Scheffer et al. (2016) showed isobaric heating of ~50 °C from 300 to 350 °C at 5–8.5 kbar. Finally, on Tinos, Parra et al. (2002) proposed drastic isobaric heating of 150–300 °C between ~370 and 550 °C at a slightly higher pressure of ~9 kbar.In general, all these estimates have in common that isobaric heating took place in the middle crust (at 25–35 km depth).

Interestingly, isobaric heating in Syros is reported from the lowermost CBU sequence, as observed in Naxos. For Andros, Syros and Tinos, the timing of the isobaric heating is only broadly estimated between the Eocene and the Oligocene/Miocene (Huet et al., 2015; Laurent et al., 2018; Parra et al., 2002). However, for Samos, it is suggested to have occurred between >35 and 18–25 Ma (Ring et al., 1999). The latter age is slightly older but broadly in agreement with our estimate for isobaric heating on Naxos.

On Naxos, isobaric heating occurred below the upper CBU section that thickened during decompression, strongly suggesting that there is a causal relation between decompressional thickening of the upper CBU section during thrusting of the CBU onto the Cycladic basement in controlling subsequent isobaric heating in the lower half of the CBU sequence. Vanderhaeghe et al. (2007) and Vanderhaeghe (2012) proposed that thermal relaxation following tectonic accretion of the orogenic wedge casued heating of the evolving Cycladic orogen. Tectonic accretion and HP metamorphism in the Cyclades lasted until about 30 Ma (Ring et al., 2007, 2011). We consider it possible that this thermal

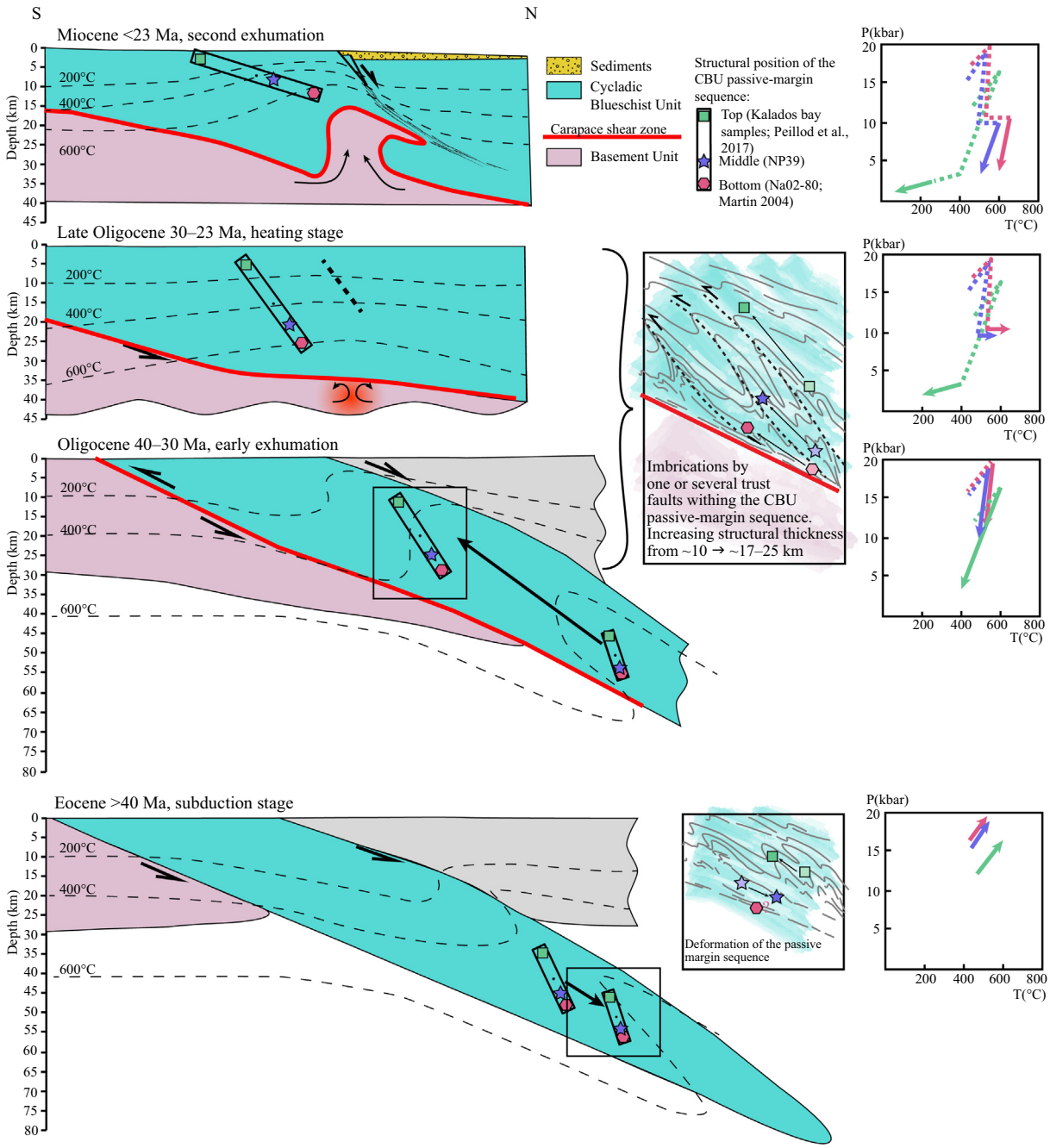

Fig. 10. Proposed structural thickness evolution of CBU sequence on Naxos. Location and isotherms constrained from P-T path for top, middle and the bottom of sequence displayed on right (same colour code as Fig. 10). Carapace shear zone is shown by red line; note that doming of carapace shear zone and migmatite dome in uppermost panel enhanced by *E*-W shortening perpendicular to cross-sectional sketch.

relaxation following crustal thickening caused a heating pulse during a tectonically quiescent period on Naxos before lithospheric extension commened by 23–20.5 Ma.

7. Conclusion

Our study shows that the bottom half of CBU passive-margin sequence on Naxos experienced a different P-T path than the top of the unit. The top of the CBU section was exhumed in one seemingly continuous go into the uppermost middle crust beneath a normal fault at the top of the extruding wedge and underwent mid-Oligocene greenschist-facies equilibration. In contrast, the bottom half of the CBU above a basal thrust fault of the extruding wedge was exhumed only to about 35 km after its HP overprint. This bottom section of the CBU was thrust onto the Cycladic basement and finally emplaced above it by ~30 Ma, a time that marks the end of crustal thickening and HP metamorphism in the Cyclades. At about this time, the bottom half of the CBU started to heat-up isobarically, probably controlled by its position above the thermally relaxing radiogenic basement.

Declaration of Competing Interest

None.

Acknowledgements

This research did not receive any specific grant from funding agencies in the public, commercial, or not-for-profit sectors. We appreciate reviews by Olivier Vanderhaeghe and an anonymous referee, which helped us to improve the manuscript.

Appendix A. Supplementary data

Supplementary data to this article can be found online at https://doi.org/10.1016/j.lithos.2021.106043.

References

Andriessen, P.A.M., Boelrijk, N.A.I.M., Hebeda, E.H., Priem, H.N.A., Verdurnen, E.A.T., Verschure, R.H., 1979. Dating the events of metamorphism and granitic magmatism in the Alpine orogen of Naxos (Cyclades, Greece). Contrib. Mineral. Petrol. 69, 215–225. https://doi.org/10.1007/BF00372323.

Angel, R.J., Murri, M., Mihailova, B., Alvaro, M., 2019. Stress, strain and Raman shifts. Zeitschrift fur Kristallographie - Cryst. Mater. 234, 129–140. https://doi.org/10.1515/zkri-2018-2112.

Angelier, J., Lybéris, N., Le Pichon, X., Barrier, E., Huchon, P., 1982. The tectonic development of the Hellenic arc and the sea of Crete: a synthesis. Tectonophysics 86, 159–196.

Aravadinou, E., Xypolias, P., 2017. Evolution of a passive crustal-scale detachment (Syros, Aegean region): Insights from structural and petrofabric analyses in the hangingwall. J. Struct. Geol. https://doi.org/10.1016/j.jsg.2017.09.008.

Avigad, D., 1998. High-pressure metamorphism and cooling on SE Naxos (Cyclades, Greece). Eur. J. Mineral. 10, 1309–1319.

Avigad, D., Garfunkel, Z., Jolivet, L., Azañón, J.M., 1997. Back arc extension and denudation of Mediterranean eclogites. Tectonics 16, 924–941. https://doi.org/10.1029/97TC02003.

Bolhar, R., Ring, U., Allen, C.M., 2010. An integrated zircon geochronological and geochemical investigation into the Miocene plutonic evolution of the Cyclades, Aegean Sea, Greece: Part 1: Geochronology. Contrib Mineral Petrol 160, 719–742. https://doi.org/10.1007/s00410-010-0504-4.

Bolhar, R., Ring, U., Ireland, T.R., 2017. Zircon in amphibolites from Naxos, Aegean Sea, Greece: origin, significance and tectonic setting. J. Metamorph. Geol. 35, 413–434. https://doi.org/10.1111/jmg.12238.

Brichau, S., Ring, U., Ketcham, R.A., Carter, A., Stockli, D., Brunel, M., 2006. Constraining the long-term evolution of the slip rate for a major extensional fault system in the Central Aegean, Greece, using thermochronology. Earth Planet. Sci. Lett. 241, 293–306. https://doi.org/10.1016/j.epsl.2005.09.065.

Bucher, K., Grapes, R., 2011. Petrogenesis of metamorphic rocks. Springer Sci. Bus. Media https://doi.org/10.1007/978-3-540-74169-5.

Buick, I.S., 1991. The late Alpine evolution of an extensional shear zone, Naxos, Greece. J. Geol. Soc. 148, 93–103. https://doi.org/10.1144/gsjgs.148.1.0093.

Buick, I.S., Holland, B., 1989. The P-T-t path associated with crustal extension, Naxos, Cyclades, Greece. Geol. Soc. Lond., Spec. Publ. 43, 365–369. https://doi.org/10.1144/GSL.SP.1989.043.01.32.

Bukała, M., Barnes, C.J., Jeanneret, P., Hidas, K., Mazur, S., Almqvist, B.S.G., Kośmińska, K., Klonowska, I., Šurka, J., Majka, J., 2020. Brittle deformation during eclogitization of early Paleozoic Blueschist. Front. Earth Sci. 8, 1–17. https://doi.org/10.3389/feart.2020.594453.

Cao, S., Neubauer, F., Bernroider, M., Genser, J., Liu, J., Friedl, G., 2017. Low-grade retrogression of a high-temperature metamorphic core complex : Naxos, Cyclades, Greece. Geol. Soc. Am. 129, 93–117. https://doi.org/10.1130/B31502.1.

Cao, S., Neubauer, F., Bernroider, M., Genser, J., 2018. Eocene high-pressure metamorphism and Oligocene retrogression on Naxos, Cyclades, Greece: significance for Aegean tectonics and 40Ar/39Ar dating in polyphase metamorphic rocks. Tectonophysics 745, 66–94. https://doi.org/10.1016/j.tecto.2018.08.009.

Chatzaras, V., Xypolias, P., Doutos, T., 2006. Exhumation of high-pressure rocks under continuous compression: a working hypothesis for the southern Hellenides (Central Crete, Greece). Geol. Mag. 143, 859–876. https://doi.org/10.1017/S0016756806002585.

de Capitani, C., Brown, T.H., 1987. The computation of chemical equilibrium in complex systems containing non-ideal solutions. Geochim. Cosmochim. Acta 51, 2639–2652.

de Capitani, C., Petrakakis, K., 2010. The computation of equilibrium assemblage diagrams with Theriak/Domino software. Am. Mineral. 95, 1006–1016. https://doi.org/10.2138/am.2010.3354.

Duchêne, S., Aïssa, R., Vanderhaeghe, O., 2006. Pressure-temperature-time evolution of metamorphic rocks from Naxos (Cyclades, Greece): Constraints from thermobarometry and Rb/Sr dating. Geodin. Acta 19, 299–319. https://doi.org/10.3166/ga.19.301-321.

England, P.C., Thompson, A.B., 1984. Pressure-temperature-time paths of regional metamorphism I. Heat transfer during the evolution of thickened continental crust. J. Petrol. 25, 894–928.

Fassoulas, C., 1998. The structural evolution of Central Crete: Insight into the tectonic evolution of the South Aegean (Greece). J. Geodyn. 27, 23–43. https://doi.org/10.1016/S0264-3707(97)00026-4.

Gautier, P., Brun, J.P., Jolivet, L., 1993. Structure and kinematics of upper Cenozoic extensional detachment on Naxos and Paros (Cyclades Island, Greece). Tectonics 12, 1180–1194.

George, F.R., Gaidies, F., 2017. Characterisation of a garnet population from the Sikkim Himalaya: insights into the rates and mechanisms of porphyroblast crystallisation. Contrib. Mineral. Petrol. 172. https://doi.org/10.1007/s00410-017-1372-y.

Gerya, T.V., Stöckhert, B., Perchuk, A.L., 2002. Exhumation of high-pressure metamorphic rocks in a subduction channel: a numerical simulation. Tectonics 21. https://doi.org/10.1029/2002tc001406 6-1-6–19.

Gessner, K., Ring, U., Passchier, C.W., Güngör, T., 2001. How to resist subduction: evidence for large-scale out-of-sequence thrusting during Eocene collision in Western Turkey. J. Geol. Soc. 158, 769–784. https://doi.org/10.1144/jgs.158.5.769.

Glazner, A.F., Bartley, J.M., 1985. Evolution of lithospheric strength after thrusting. Geology 13, 42–45.

Glodny, J., Ring, U., Kühn, A., 2008. Coeval high-pressure metamorphism, thrusting, strike-slip, and extensional shearing in the Tauern Window, Eastern Alps. Tectonics 27. https://doi.org/10.1029/2007TC002193 (27 pp).

Huet, B., Le Pourhiet, L., Labrousse, L., Burov, E.B., Jolivet, L., 2011. Formation of metamorphic core complex in inherited wedges: a thermomechanical modelling study. Earth Planet. Sci. Lett. 309, 249–257. https://doi.org/10.1016/j.epsl.2011.07.004.

Huet, B., Labrousse, L., Monié, P., Malvoisin, B., Jolivet, L., 2015. Coupled phengite 40Ar-39Ar geochronology and thermobarometry: P-T-t evolution of Andros Island (Cyclades, Greece). Geol. Mag. 152, 711–727. https://doi.org/10.1017/S0016756814000661.

Jacobshagen, V., Dürr, S., Kockel, F., Makris, J., Meyer, W., Röwer, P., Schröder, B., Seidel, E., Wachendorf, H., Dornsiepen, U., Giese, P., Wallbrecher, E., 1986. Geologie von Griechland. Berträge zur Regionalen Geologie der Erde, 19, Borntraeger, Berlin-Stuttgart, Germany (363 pp).

Jansen, J.B.H., Schuiling, R.D., 1976. Metamorphism on Naxos petrology and geothermal gradient. Am. J. Sci. 276, 1225–1253. https://doi.org/10.2475/ajs.276.10.1225.

John, B.E., Howard, K.a., 1995. Rapid extension recorded by cooling-age patterns and brittle deformation, Naxos, Greece. J. Geophys. Res. 100, 9969.

Keay, S., Lister, G., Buick, I., 2001. The timing of partial melting, Barrovian metamorphism and granite intrusion in the Naxos metamorphic core complex, Cyclades, Aegean Sea, Greece. Tectonophysics 342, 275–312. https://doi.org/10.1016/S0040-1951(01)00168-8.

Kruckenberg, S.C., Ferré, E.C., Teyssier, C., Vanderhaeghe, O., Whitney, D.L., Seaton, N.C.A., Skord, J.A., 2010. Viscoplastic flow in migmatites deduced from fabric anisotropy: An example from the Naxos dome, Greece. J. Geophys. Res. Solid Earth 115. https://doi.org/10.1029/2009JB007012 (18 pp).

Kruckenberg, S.C., Vanderhaeghe, O., Ferré, E.C., Teyssier, C., Whitney, D.L., 2011. Flow of partially molten crust and the internal dynamics of a migmatite dome, Naxos, Greece. Tectonics 30, 1–24. https://doi.org/10.1029/2010TC002751.

Lamont, T.N., Searle, M.P., Waters, D.J., Roberts, N.M.W., Palin, R.M., Smye, A., Dyck, B., Gopon, P., Weller, O.M., St-onge, M.R., 2019. Compressional origin of the Naxos metamorphic core complex, Greece: Structure, petrography, and thermobarometry. Geol. Soc. Am. Bull., 1–49 https://doi.org/10.1130/B31978.1/4719075/b31978.pdf.

Laurent, V., Lanari, P., Naïr, I., Augier, R., Lahfid, A., Jolivet, L., 2018. Exhumation of eclogite and blueschist (Cyclades, Greece): Pressure-temperature evolution determined by thermobarometry and garnet equilibrium modelling. J. Metamorph. Geol. Accepted Artic. https://doi.org/10.1111/jmg.12309.

Linnros, H., Hansman, R., Ring, U., 2019. The 3D geometry of the Naxos detachment fault and the three-dimensional tectonic architecture of the Naxos metamorphic core complex, Aegean Sea, Greece. Int. J. Earth Sci. 108, 287–300. https://doi.org/10.1007/s00531-018-1654-2.

Lisker, S., 1993. The Tectonosedimentary Upper Units of the Cyclades (Aegean Sea, Greece) A Paleogeographic and Tectonic Reconstruction. MSc-Thesis. Hebrew University, Jerusalem.

Lister, G.S., Forster, M.A., 1996. Inside the Aegean Metamorphic Core Complexes : A Field Trip Guide Illustrating the Geology of 41–46. https://doi.org/10.3809/doi.

Mancktelow, N., Zwingmann, H., Mulch, A., 2016. Timing and conditions of clay fault gouge formation on the Naxos detachment (Cyclades, Greece). Tectonics 35, 2334–2344. https://doi.org/10.1002/2016TC004251.

Martin, L., 2004. Signification des Âges U-Pb sur Zircon dans L'histoire Métamorphique de Naxos et Ikaria (Cyclades, Grèce). Université Henri Poincaré.

Martin, L., Duchêne, S., Deloule, E., Vanderhaeghe, O., 2006. The isotopic composition of zircon and garnet: a record of the metamorphic history of Naxos, Greece. Lithos 87, 174–192. https://doi.org/10.1016/j.lithos.2005.06.016.

Okrusch, M., Bröcker, M., 1990. Eclogites associated with high-grade blueschists in the Cyclades archipelago, Greece: a review. Eur. J. Mineral. 2, 451–478.

Parra, T., Vidal, O., Jolivet, L., 2002. Relation between the intensity of deformation and retrogression in blueschist metapelites of Tinos Island (Greece) evidenced by chlorite-mica local equilibria. Lithos 63, 41–66. https://doi.org/10.1016/S0024-4937(02)00115-9.

Peillod, A., 2018. The Metamorphic History of Naxos (Central Cyclades, Greece): Deciphering the Oligocene and Miocene Exhumation Events. Stockholm University.

Peillod, A., Ring, U., Glodny, J., Skelton, A., 2017. An Eocene/Oligocene blueschist−/greenschist facies P–T loop from the Cycladic Blueschist Unit on Naxos Island, Greece: Deformation-related re-equilibration vs. thermal relaxation. J. Metamorph. Geol. 35, 805–830. https://doi.org/10.1111/jmg.12256.

Peillod, A., Glodny, J., Ring, U., Skelton, A., Villa, I.M., 2019. Sr and Ar diffusion systematics in polygenetic white micas from Naxos. GeoMünster 2019.

Peillod, A., Ring, U., Tehler, E., 2021. Quo vadis Zeus - Is there a Zas Shear Zone on Naxos Island, Aegean Sea, Greece ? A Review of Metamorphic History and New Kinematic Data. Tectonophysics Accepted Pending Revisions.

Poulaki, E.M., Stockli, D.F., Flansburg, M.E., Soukis, K., 2019. Zircon U - Pb chronostratigraphy and provenance of the cycladic blueschist unit and the nature of the contact with the cycladic basement on Sikinos and Ios Islands, Greece. Tectonics 38, 3586–3613. https://doi.org/10.1029/2018TC005403.

Ring, U., Glodny, J., 2010. No need for lithospheric extension for exhuming (U)HP rocks by normal faulting. J. Geol. Soc. 167, 225–228. https://doi.org/10.1144/0016-76492009-134.

Ring, U., Glodny, J., Will, T., Thomson, S., 2010. The Hellenic Subduction System: High-Pressure Metamorphism, Exhumation, Normal Faulting, and Large-Scale Extension. Annual Review of Earth and Planetary Sciences 38, 45–76. https://doi.org/10.1146/annurev.earth.050708.170910.

Ring, U., Reischmann, T., 2002. The weak and superfast Cretan detachment, Greece: exhumation at subduction rates in extruding wedges. J. Geol. Soc. 159, 225–228.

Ring, U., Laws, S., Bernet, M., 1999. Structural analysis of a complex nappe sequence and late-orogenic basins from the Aegean Island of Samos, Greece. J. Struct. Geol. 21, 1575–1601. https://doi.org/10.1016/S0191-8141(99)00108-X.

Ring, U., Glodny, J., Will, T., Thomson, S., 2007. An Oligocene extrusion wedge of blueschist-facies nappes on Evia, Aegean Sea, Greece: implications for the early exhumation of high-pressure rocks. J. Geol. Soc. 164, 637–652. https://doi.org/10.1144/0016-76492006-041.

Ring, U., Glodny, J., Will, T.M., Thomson, S., 2011. Normal faulting on Sifnos and the South Cycladic Detachment System, Aegean Sea, Greece. J. Geol. Soc. 168, 751–768. https://doi.org/10.1144/0016-76492010-064.

Ring, U., Glodny, J., Peillod, A., Skelton, A., 2018. The timing of high-temperature conditions and ductile shearing in the footwall of the Naxos extensional fault system, Aegean Sea, Greece. Tectonophysics 745, 366–381. https://doi.org/10.1016/j.tecto.2018.09.001.

Ring, U., Pantazides, H., Glodny, J., Skelton, A., 2020. Forced return flow deep in the subduction channel, Syros, Greece. Tectonics 39. https://doi.org/10.1029/2019TC005768.

Rubatto, D., Hermann, J., 2001. Exhumation as fast as subduction? Geology 29, 3–6. https://doi.org/10.1130/0091-7613(2001)?029<0003:EAFAS>?2.0.CO.

Scheffer, C., Vanderhaeghe, O., Lanari, P., Tarantola, A., Ponthus, L., Photiades, A., France, L., 2016. Syn- to post-orogenic exhumation of metamorphic nappes: Structure and thermobarometry of the western Attic-Cycladic metamorphic complex (Lavrion, Greece). J. Geodyn. 96, 174–193. https://doi.org/10.1016/j.jog.2015.08.005.

Semprich, J., Simon, N.S.C., Podladchikov, Y.Y., 2010. Density variations in the thickened crust as a function of pressure, temperature, and composition. Int. J. Earth Sci. 99, 1487–1510. https://doi.org/10.1007/s00531-010-0557-7.

Seward, D., Vanderhaeghe, O., Siebenaller, L., Thomson, S., Hibsch, C., Zingg, A., Holzner, P., Ring, U., Duchêne, S., 2009. Cenozoic tectonic evolution of Naxos Island through a multi-faceted approach of fission-track analysis. Geol. Soc. Lond., Spec. Publ. 321, 179–196. https://doi.org/10.1144/SP321.9.

Stipp, M., Stünitz, H., Heilbronner, R., Schmid, S.M., 2002. The eastern Tonale fault zone: a "natural laboratory" for crystal plastic deformation of quartz over a temperature range from 250 to 700 °C. J. Struct. Geol. 24, 1861–1884. https://doi.org/10.1016/S0191-8141(02)00035-4.

Thomas, J.B., Watson, E.B., Spear, F.S., Wark, D.A., 2015. TitaniQ recrystallized: experimental confirmation of the original Ti-in-quartz calibrations. Contrib. Mineral. Petrol. 169. https://doi.org/10.1007/s00410-015-1120-0.

Trotet, F., Jolivet, L., Vidal, O., 2001. Tectono-metamorphic evolution of Syros and Sifnos islands (Cyclades, Greese). Tectonophysics 338, 179–206. https://doi.org/10.1016/S0040-1951(01)00138-X.

Vanderhaeghe, O., 2004. Structural development of the Naxos migmatite dome. Geol. Soc. Am. Spec. Pap. 380, 211–227. https://doi.org/10.1130/0-8137-2380-9.211.

Vanderhaeghe, O., 2012. The thermal-mechanical evolution of crustal orogenic belts at convergent plate boundaries: a reappraisal of the orogenic cycle. J. Geodyn. 56–57, 124–145. https://doi.org/10.1016/j.jog.2011.10.004.

Vanderhaeghe, O., Hibsch, C., Siebenaller, L., Martin, L., Duchêne, S., de Blanquat, S.M., Kruckenberg, S., Fotiadis, A., 2007. GUIDE, Naxos Field, Penrose Conference Extending a Continent.

Vanderhaeghe, O., Kruckenberg, S.C.C., Gerbault, M., Martin, L., Duchêne, S., Deloule, E., 2018. Crustal-scale convection and diapiric upwelling of a partially molten orogenic root (Naxos dome, Greece). Tectonophysics 746, 459–469. https://doi.org/10.1016/j.tecto.2018.03.007.

Warren, C.J., Hanke, F., Kelley, S.P., 2012. When can muscovite 40Ar/ 39Ar dating constrain the timing of metamorphic exhumation? Chem. Geol. 291, 79–86. https://doi.org/10.1016/j.chemgeo.2011.09.017.

Whitney, D.L., Evans, B.W., 2010. Abbreviations for names of rock-forming minerals. Am. Mineral. 95, 185–187. https://doi.org/10.2138/am.2010.3371.

Wijbrans, J.R., McDougall, I., 1986. 40Ar/39Ar dating of white micas from an Alpine high-pressure metamorphic belt on Naxos (Greece): the resetting of the argon isotopic system. Contrib. Mineral. Petrol. 93, 187–194. https://doi.org/10.1007/BF00371320.

Wijbrans, J.R., McDougall, I., 1988. Metamorphic evolution of the attic Cycladic Metamorphic Belt on Naxos (Cyclades, Greece) utilizing 40Ar/39Ar age spectrum measurements. J. Metamorph. Geol. 6, 571–594.

Wu, C.M., Chen, H.X., 2015. Revised Ti-in-biotite geothermometer for ilmenite- or rutile-bearing crustal metapelites. Sci. Bull. 60, 116–121. https://doi.org/10.1007/s11434-014-0674-y.

Xypolias, P., Kokkalas, S., Skourlis, K., 2003. Upward extrusion and subsequent transpression as a possible mechanism for the exhumation of HP/LT rocks in Evia Island (Aegean Sea, Greece). J. Geodyn. 35, 303–332. https://doi.org/10.1016/S0264-3707(02)00131-X.